POLITECNICO DI TORINO
Repository ISTITUZIONALE

A method for spatially resolved techno-economic assessment of offshore wind-to-hydrogen systems: A northern Adriatic Sea case study

*Original*
A method for spatially resolved techno-economic assessment of offshore wind-to-hydrogen systems: A northern Adriatic Sea case study / Ferrarese, A., Marocco, P., Mattiazzo, G., Santarelli, M.. - In: ENERGY CONVERSION AND MANAGEMENT. - ISSN 0196-8904. - ELETTRONICO. - 350:(2026). [10.1016/j.enconman.2025.120948]

*Availability:*
This version is available at: 11583/3008545 since: 2026-03-10T16:21:31Z

*Publisher:*
Elsevier

*Published*
DOI:10.1016/j.enconman.2025.120948

*Terms of use:*

This article is made available under terms and conditions as specified in the corresponding bibliographic description in the repository

*Publisher copyright*

(Article begins on next page)

25 November 2026

Energy Conversion and Management 350 (2026) 120948



Contents lists available at ScienceDirect

Energy Conversion and Management

journal homepage: www.elsevier.com/locate/enconman

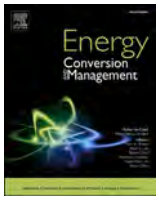



# A method for spatially resolved techno-economic assessment of offshore wind-to-hydrogen systems: A northern Adriatic Sea case study

Alberto Ferrarese [a,*], Paolo Marocco [a], Giuliana Mattiazzo [b], Massimo Santarelli [a]

[a] Department of Energy, Politecnico di Torino, Corso Duca degli Abruzzi 24, 10129 Torino, Italy
[b] Department of Mechanical and Aerospace Engineering, Politecnico di Torino, Corso Duca degli Abruzzi, 24,10129 Torino, Italy

ARTICLE INFO

*Keywords:*
Offshore wind
GIS
Hydrogen
Electrolyzer
Space eligibility assessment
Techno-economic analysis

ABSTRACT

The evolving global energy landscape increasingly positions hydrogen as a key element in the transition toward a sustainable, carbon–neutral society. Concurrently, offshore wind renewable energy offers significant untapped potential. Using it to produce green hydrogen offshore presents a promising pathway to efficiently harness this resource for large-scale hydrogen generation. This work proposes a method for a georeferenced information system-based techno-economic assessment of hydrogen producibility (kt/year) and levelized cost at ports (€/kg), assuming an offshore system powered by wind energy that delivers hydrogen onshore via a dedicated pipeline. The flexibility of the method allows for its application across different offshore domains with high reproducibility. The techno-economic model is applied to a case study covering the northern Adriatic Sea, where the estimated hydrogen producibility ranges between 0.45 and 1.25 kt/year. This domain also serves as the basis for sensitivity analyses, which explore optimal design assumptions for the electrolyzer system, including efficiency and sizing. The results underscore the importance of a preliminary spatial eligibility assessment and the adequacy of approximating electrolyzer variable efficiency with its average value. Despite some periods of low utilization, the cost-optimal electrolyzer size resulted equal to the installed capacity of the offshore wind farm across all locations. Key cost-efficient hotspots are identified in both shallow and deep waters, with offshore levelized cost of electricity between 60 and 140 €/MWh, and levelized costs of hydrogen between 5 and 6 €/kg. These findings highlight the spatial dependence of hydrogen cost on critical parameters, particularly water depth and distance to ports.

## 1. Introduction

Offshore wind is among the most promising and favorable renewable energy sources. Offshore areas often provide a more favourable environment for harvesting renewable electricity from wind energy, as the sea surface is smoother than onshore terrains, ensuring stronger and more consistent winds even at relatively low elevations. This results in higher capacity factors and output for offshore wind farms compared to onshore ones. Moreover, given the physical, anthropic, and spatial planning constraints, the sea surface available for energy exploitation is generally larger than on land, and, when minimum distances from the coastline are respected, offshore projects tend to achieve greater public acceptance. By the end of 2023, roughly 74 GW of offshore wind capacity had been deployed worldwide [1], with projections indicating growth to 212 GW by 2030, nearly quadrupling the expansion observed during 2018–2023 period [2].

At the same time, hydrogen, which does not emit carbon dioxide ($CO_2$) or air pollutants when used, is attracting renewed and rapidly growing global attention [3]. The recent global energy crisis has further accelerated the push for low-emission hydrogen, given its potential to enhance energy security [4]. In addition to traditional applications such as refining, ammonia, methanol and other chemicals production, electronics, glassmaking, and metal processing [4], many countries have introduced strategies to promote hydrogen as a key energy carrier [5]. Between 2020 and 2022, the number of governments developing hydrogen strategies more than doubled, from 18 [6] to 39 [7]. Hydrogen is also expected to play a central role in a wide range of emerging applications, either as a fuel or an energy storage for industry, transport, power and buildings sectors [3]. Examples of competitive hydrogen uses in the coming years include: industrial heating, where hydrogen will be the only viable decarbonizing option in some cases [6]; replacement of fossil fuels in hard-to-abate and carbon intensive industrial processes,

* Corresponding author.
*E-mail address:* alberto.ferrarese@polito.it (A. Ferrarese).

https://doi.org/10.1016/j.enconman.2025.120948
Received 23 May 2025; Received in revised form 9 December 2025; Accepted 11 December 2025
Available online 29 December 2025
0196-8904/© 2025 The Author(s). Published by Elsevier Ltd. This is an open access article under the CC BY-NC-ND license (http://creativecommons.org/licenses/by-nc-nd/4.0/).

**Table 1**
Literature review on the articles evaluating the levelized cost of hydrogen (LCOH) produced using renewable electricity generated by offshore wind farms.

| Reference | | | LCOE | | | LCOH | | | | GIS | Place |
|---|---|---|---|---|---|---|---|---|---|---|---|
| Meier K. et al. | [26] | 2014 | | – | | 6.30–106.10 | €/kg | [a] | (offs., PEMEL) | | Europe: North Sea |
| | | | | | | 5.17–106.15 | €/kg | [a] | (offs., SOEL) | | |
| Song et al. | [14] | 2021 | | – | | 2–6 | $/kg | [a] | (ons., PEMEL, SOEL, AEL, 2030–2050) | x | China |
| Singlitico et al. | [24] | 2021 | 40–100 | €/MWh | [a] | 2.25–15 | €/kg | [a] | (offs., PEMEL, SOEL, AEL) | | Europe: North Sea |
| Scolaro et al. | [27] | 2021 | 70 | €/MWh | [b] | 4.9–7.25 | €/kg | [b] | (offs., PEMEL) | | Europe: North Sea |
| Franco et al. | [28] | 2021 | 20–70 | €/MWh | [b] | 2.17–10.5 | €/kg | [a] | (offs., PEMEL) | | Europe (General theoretical place at varying distance from the coast) |
| Lucas et al. | [16] | 2022 | | – | | 2.5–11.5 | €/kg | [a] | (ons., PEMEL) | | Europe: Portugal, Viana do Castelo |
| Dohyung et al. | [29] | 2022 | | – | | 13.811–16 | $/kg | [a] | (dist., PEMEL) | | Not defined (General theoretical place at varying distance from the coast) |
| | | | | | | 13.847–16 | $/kg | [a] | (cent-offs.., PEMEL) | | |
| | | | | | | 14.584–19 | $/kg | [a] | (ons., PEMEL) | | |
| Komorowska et al. | [22] | 2023 | | – | | 3.59–3.71 | €/kg | [a] | (ons., PEMEL, 2030) | x | Europe: Poland |
| | | | | | | 2.05–2.15 | €/kg | [a] | (ons., PEMEL, 2050) | | |
| Giampieri et al. | [18] | 2023 | | – | | 3.43–33.24 | £/kg | [a] | (offs., PEMEL, 2025) | | Europe: UK |
| | | | | | | 2.37–30.40 | £/kg | [a] | (offs., PEMEL, 2030) | | |
| | | | | | | 1.22–28.17 | £/kg | [a] | (offs., PEMEL, 2050) | | |
| | | | | | | 4.33–268.8 | £/kg | [a] | (ons., PEMEL, 2025) | | |
| | | | | | | 2.97–184 | £/kg | [a] | (ons., PEMEL, 2030) | | |
| | | | | | | 1.55–179.6 | £/kg | [a] | (ons., PEMEL, 2050) | | |
| | | | | | | 4.59–25.27 | £/kg | [a] | (offs., liq., PEMEL,2025) | | |
| | | | | | | 2.95–11.74 | £/kg | [a] | (offs., liq., PEMEL, 2030) | | |
| | | | | | | 2.07–6.66 | £/kg | [a] | (offs., liq., PEMEL, 2050) | | |
| Rogeau et al. | [19] | 2023 | | – | | 4.5–9.5 | €/kg | [a] | (2020) | x | Europe with insights for Denmark, Sweden, Norway, Netherland, Poland, France, Germany, UK, Ireland |
| | | | | | | 2.25–7.25 | €/kg | [a] | (2030) | | |
| | | | | | | 1.25–5.00 | €/kg | [a] | (2050) | | |
| Dinh et al. | [30] | 2023 | | – | | 4–9.5 | €/kg | [a] | (ons., PEMEL) | x | Europe: Irish coasts, Irish Sea |
| Dinh et al. | [17] | 2023 | | – | | 2–5.8 | €/kg | [a] | (cent-offs., PEMEL, 2030) | x | Europe: Irish coasts, Irish Sea |
| Ding et al. | [23] | 2024 | | – | | 10.3–22.0 | $/kg | [a] | (cent-offs., PEMEL) | x | Asia: Taiwan |
| | | | | | | 10.3–22.1 | $/kg | [a] | (dist., PEMEL) | | |
| | | | | | | 11.3–22.6 | $/kg | [a] | (ons., PEMEL) | | |
| Zhou et al. | [21] | 2024 | | – | | 7.13 | $/kg | [a] | (cent-offs., PEMEL, 2025) | x | Asia: China (Chinese coasts and Taiwan) |
| | | | | | | 5.28 | $/kg | [a] | (cent-offs., PEMEL, 2030) | | |
| | | | | | | 3.77 | $/kg | [a] | (cent-offs., PEMEL, 2050) | | |
| Vidas et al. | [20] | 2024 | 110 | €/MWh | [b] | 10.48 | €/kg | [b] | Average (PEMEL) | x | Europe: Italy Europe: Portugal |
| | | | 435 | €/MWh | [b] | 15.81 | €/kg | [b] | Average (PEMEL) | | |
| Juárez-Casildo et al. | [15] | 2024 | 67.9–241.5 | $/MWh | [a] | 10–11.23 | $/kg | [a] | (cent-offs., AEL) | x | Central America: Mexico |
| | | | 65.1–214 | $/MWh | [b] | 11.53–12.83 | $/kg | [a] | (cent-offs., PEMEL) | | |
| | | | | | | 10.93 | $/kg | [a] | (ons., AEL) | | |
| | | | | | | 12.35 | $/kg | [a] | (ons., PEMEL) | | |
| Hill et al. | [31] | 2024 | 94.54 | €/MWh | [a] | 5.60–13.48 | €/kg | [a] | (cent-offs., AEL) | | Europe: UK |
| | | | | | | 7.50–15.96 | €/kg | [a] | (cent-offs., PEMEL) | | |
| | | | | | | 5.47–13.81 | €/kg | [a] | (ons., AEL) | | |

[a] at the mainland delivering point.
[b] at the production site (which for the LCOH can be either offshore or onshore).
cent-offs. = centralized-offshore production.
offs. = offshore production.
ons. = onshore production.
dist. = distributed production.
liq. = liquefied.
PEMEL = Proton Exchange Membrane Electrolyzer.
AEL = Alkaline Electrolyzer.
SOEL = Solid Oxide Electrolyzer.
LCOE = Levelized cost of electricity.
LCOH = Levelized cost of hydrogen.
GIS = Georeferenced Information System.

such as steel or chemical production [3]; production of hydrogen-based fuels (e.g. ammonia and synthetic hydrocarbons) and biofuel upgrading (e.g. hydrogenation of fats and oils) [4]; electricity storage and generation [4], where hydrogen is expected to play an increasingly systemic role in balancing the power system [3] also in off-grid and remote regions [8]; propulsion (e.g., feeding fuel cells in electric vehicles [9] or internal combustion engines [10]) for commercial vehicles, trains, and long-range transport [3] such as shipping and aviation [4] where declining equipment and refuelling costs will likely enable hydrogen to compete with other low-carbon alternatives by 2030 [6].

Nevertheless, hydrogen is not a homogeneous energy carrier, as it can be produced from a wide range of primary sources (coal, oil, natural gas, biomass, renewables, and nuclear) through diverse technologies such as reforming, gasification, electrolysis, pyrolysis, and water splitting [11]. Consequently, its carbon footprint varies significantly depending on the production pathway. To facilitate discussion, in recent years a color-code nomenclature has become increasingly common to classify different production routes [11], indicating as green hydrogen the hydrogen produced through electrolysis powered by renewable electricity [7] and thus not directly associated with greenhouse gas emissions during its production phase [5]. Meeting the Paris Agreement objectives and advancing toward a Net Zero Emissions scenario will therefore need including green hydrogen among the strategic molecules for decarbonization, requiring substantial investment in renewable electricity capacity dedicated to its production. This is why, by 2030, green hydrogen is forecast to drive 43 GW of new global renewable capacity installation [2] which is far below what should be, according to [12], i.e. 365 GW from 2021 to 2030 to meet the Net Zero Emission scenario for 2050. The International Energy Agency (IEA) estimated in 2019 that the global offshore wind technical potential is 120 TW, enough to cover 11 times the electricity demand in 2040 [13]. With such figures, the potential of offshore wind energy to meet green hydrogen ($H_2$) production targets for 2050 in the Net Zero Emission scenario is evident. Nonetheless, these estimations must be grounded in realistic assessments of resource availability, accounting for the usable sea surface dedicated to energy production and the costs at which these resources become available (i.e., levelized costs of electricity – LCOE – and hydrogen – LCOH).

In such a context, the georeferenced assessment of the offshore hydrogen producibility has gained increasing attention in recent years around the world. For instance, [14] analyzes green hydrogen production from Chinese offshore areas to meet Japanese demand at competitive prices, while [15] applies geospatial analysis to assess the decarbonization potential of offshore green hydrogen in Mexico under demand scenarios for specific applications like transportation, ammonia production, and refineries. At the same time, several studies concerning European offshore areas have assessed the potential for hydrogen producibility focusing on specific sites, national domains, or adopting a more comprehensive view of the entire European offshore region. Representative examples include: [16], which analyzes the feasibility of hydrogen production in Viana do Castelo (Portugal) using electricity from the specific 'WindFloat Atlantic' offshore wind farm and Portugal's electricity market; [17], which explores the Irish offshore potential; and [18] which evaluates the producibility potential of the entire European offshore domain.

To provide a general overview of the state of the art in this field, which focuses on hydrogen produced from offshore wind-generated electricity, Table 1 presents a comprehensive review of studies assessing hydrogen producibility and the related LCOH. It also specifies if the reported LCOE and LCOH values refer to the production point (always offshore for electricity, and either offshore or onshore for hydrogen) or to the onshore delivery point, thereby capturing differences in the power-to-gas (P2G) system designs and the system boundaries considered in each study. The columns 'GIS' (Georeferenced Information System) and 'Place' indicate whether the studies rely on georeferenced input data and whether they focus on specific sites or on spatially resolved studies (i.e., resolved across multiple units within a broader offshore discretized domain). In the latter case, output parameters are referred to as 'spatially resolved', an example being the spatially resolved LCOH, which denotes the cost of producing 1 kg of hydrogen calculated by solving the techno-economic assessment problem across all georeferenced locations within the discretized domain.

The literature review reveals that most spatially resolved studies disregard spatial eligibility constraints, providing results also for areas that, although technically promising, would not be exploitable due to physical or spatial planning restrictions. When spatial eligibility is considered, the application of different exclusion criteria can lead to substantial variations in the set of eligible sites for the same regions. For instance, [19] deemed Italian seas almost entirely ineligible, whereas [20] identified multiple viable areas for the same domain. Also, in some of these studies, well-established exclusion constraints are overlooked, such as in [21] which did not account for a minimum distance from shore which is typically included in spatial energy assessments underlying LCOH evaluations. Considering such eligibility constraints basing on environmental rules, legal issues, or public acceptance, would bring the findings close to the real-world projects.

As can be seen in Table 1, differences also arise in the selection of the electrolyzer's installation site. For instance, the centralized onshore hydrogen production design adopted by [22] was similarly considered by [14] because of its logistical advantages when exporting hydrogen to Japan. Likewise, [9] examined the Irish national domain, where electricity generated from offshore wind farms was assumed to be transmitted via subsea high-voltage cables to centralized onshore electrolyzers, a solution considered advantageous in terms of costs and ease of installation. Nevertheless, other studies have addressed the issue of determining the most suitable placement of the electrolyzer more comprehensively. This was done by comparing different P2G system designs and analyzing three possible solutions for compressed gaseous hydrogen production: centralized offshore, decentralized offshore, and centralized onshore. In the first two cases, the hydrogen is transported onshore by underwater pipelines while in the latter configuration offshore wind power is transmitted to onshore hydrogen production hubs as happened in the above cited studies. The outcomes of this analysis led [19] to identify the offshore centralized solution as the most favorable from a techno-economic perspective for the European offshore domain. Similar conclusions were drawn by [15] for the Mexican offshore area and by [23] for the Taiwan's offshore domain, leading [17] and [21] to consider this option a priori.

When considering hydrogen production via electrolysis, three main types of electrolyzers exist: proton exchange membrane electrolyzer (PEMEL), alkaline electrolyzer (AEL), and solid oxide electrolyzer (SOEL). To assess the impact of electrolyzer type, [24] analyzed different scenarios for each technology, concluding that the lowest LCOH is generally achieved with AEL, although differences compared to PEMEL and SOEL are negligible. Nonetheless, the majority of the reviewed studies have focused on PEMEL, motivated by factors similar to those highlighted in [17], including its wide operational load range (0–10 % of minimum load [25]), high flexibility in following rapid variations in renewable wind farm output, low operation temperatures and elevated operating pressure (reducing the need for additional compression when injecting hydrogen into subsea pipelines).

Among the cited studies, [20] and [21] investigated the effects of the electrolyzer size on the LCOH by using optimization algorithms for specific locations. Both the studies found that an optimal electrolyzer size slightly smaller than that of the installed wind farm exists for offshore applications. Specifically, [20] determined that this size is approximately 70 % and 90 % of the nominal power of bottom-fixed and floating offshore wind farms (OWFs), respectively. However, neither study considered the specific cost of the electrolyzer as a function of its size. Instead, they used a fixed specific cost, which could significantly affect optimization outcomes when minimizing the LCOH.

Further methodological differences in literature involve hydrogen

producibility modeling. Analytical approaches, generally requiring less computational effort and relying on functional representations of turbine power curves and Weibull wind speed distributions, were adopted by [17] and extended by [21] to three-dimensional spatio-temporal domains. In contrast, other studies like [23], employed a discrete approach, summing hourly energy contributions. Unlike the other mentioned articles, [20] applied a full-load hours (FLH)-based model dependent on existing capacity factor (CF) maps and specific wind turbines, which restricted the turbine to be used for the study to those used in CF assessments. Moreover, [22] adopted a Monte Carlo-based approach to generate the input data, at the expense of the reliability offered by real-world data. Finally, only [23] incorporated a variable efficiency function for the electrolyzer.

Building on this discussion, the present study aims to:

- provide the scientific community with a GIS-based method for assessing spatially resolved producibility and LCOH of offshore green hydrogen, designed for reproducibility through open-source tools and data while ensuring low computational cost (hence the choice of an analytical approach);
- investigate the effects of a georeferenced, well-established set of objective spatial ineligibility constraints, along with P2G system design variables, on the near-real-world availability of offshore areas for hydrogen production;
- shed light on the influence of the electrolyzer size on the LCOH through a sensitivity analysis aimed at identifying the cost-optimal design point, considering the size cost effects on the electrolyzer related costs.

In order to generate accurate insights into the impact of electrolyzer design variables on LCOH and producibility, special emphasis is placed on assumptions concerning electrolyzer design in both cost and producibility models. Specifically, this study compares constant-efficiency and variable-efficiency representations of electrolyzer performance and, unlike previous studies, incorporates a size-dependent cost function into the electrolyzer cost model. The method is applied to a demonstrative case study evaluating spatially resolved LCOH in the northern Adriatic Sea, a region that has thus far received limited attention in this research field. Here, an additional focus is placed on the potential use of existing gas pipelines for transporting pure hydrogen, since, as highlighted in [3], the progressive uptake of hydrogen solutions can also lead to repurposing or re-using parts of the existing natural gas infrastructure, helping to avoid stranded pipeline assets.

## 2. Methods

In this section, the general theoretical method developed is presented. It begins with an overview of the objectives (*Subsection 2.1*) and the georeferenced datasets required (*Subsection 2.2*). The section then proceeds to describe the characteristics of the two main steps of the method: the pre-processing of georeferenced data through an eligibility analysis aimed at optimizing the computational domain (*Subsection 2.3*); and the subsequent techno-economic assessment, detailed in the following subsections. The models adopted for the design of the offshore power-to-gas (P2G) system, the estimation of energy and hydrogen producibility, and the corresponding costs evaluation are presented in *Subsections 2.4, 2.5*, and *2.6*, together with specifications for all the P2G system components. These subsections also present the main equations used in the models, with particular emphasis on those involving georeferenced data (always indicated with an asterisk). Finally,

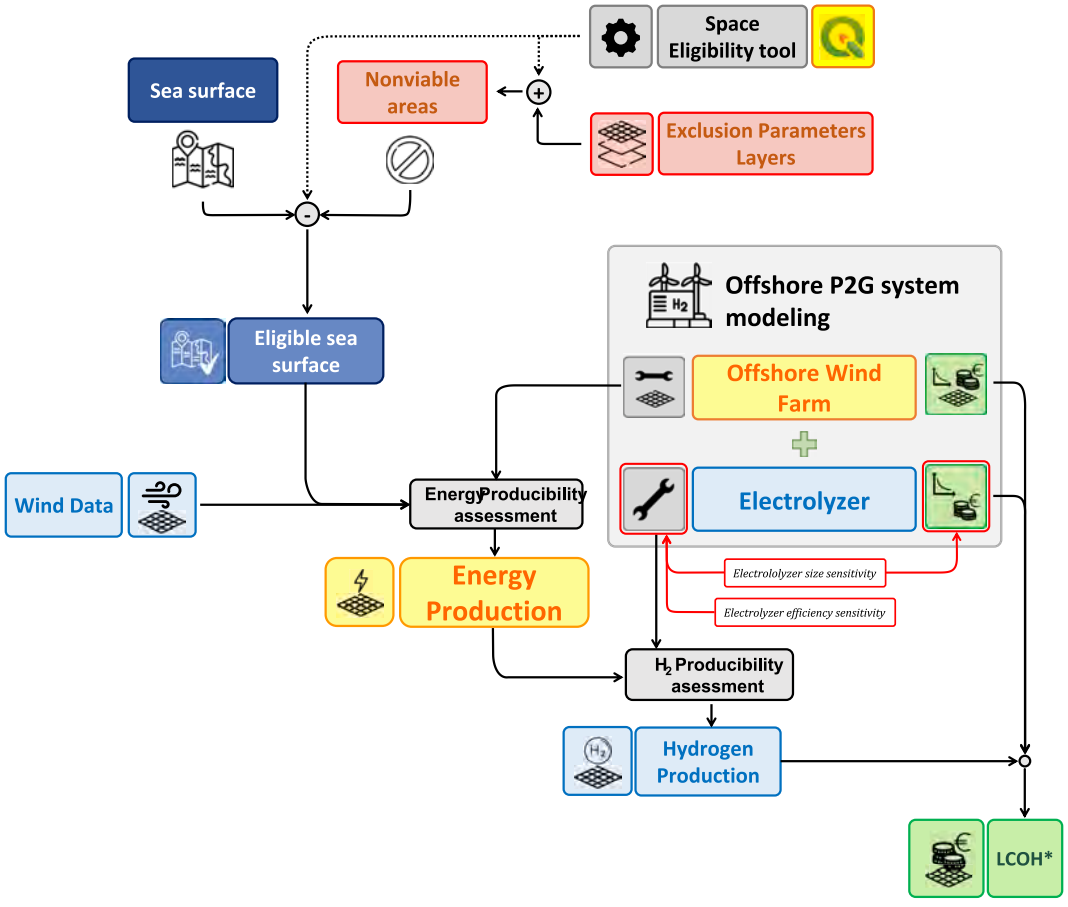


**Fig. 1.** Schematic of the entire workflow of the model (dashed line: application of the tool).

*Subsections 2.7* and *2.8* illustrate the specific methods and assumptions employed to carry-out the techno-economic assessment and the sensitivity analyses in the demonstrative case study of the northern Adriatic offshore area.

A detailed legend of the nomenclature used in this work, along with additional specifications on the techno-economic model equations not reported here for brevity, are provided in the Supplementary Material.

### 2.1. Objective

The objective of the method is to develop a detailed techno-economic model of a green $H_2$ production hub to support the spatially resolved assessment of LCOH delivered at the nearest suitable port, with the pipeline inside the system boundary (see Fig. 1). The LCOH is defined as follows:

$$LCOH^* = \frac{CAPEX^*_{sys} + OPEX^*_{sys} + DECEX^*_{sys}}{THP^*} = \frac{C^*_{sys}}{THP^*} \quad (1)$$

where $CAPEX^*_{sys}$, $OPEX^*_{sys}$ and $DECEX^*_{sys}$ represent the actualized space-dependent capital expenditures (CAPEX), operational expenditures (OPEX), decommissioning expenditures (DECEX), respectively; $C^*_{sys}$ is the total cost of the P2G system (including pipeline); and $THP^*$ denotes the total $H_2$ production of the system. In the above equation, and throughout this study, the asterisk (*) denotes a spatially dependent variable. The method developed to address this estimation is specifically designed to deliver reliable results aimed primarily at identifying areas that are techno-economically suitable for offshore hydrogen production. These areas can then be further examined in subsequent studies, including energy system modelling or detailed site-selection analyses for the installation of P2G systems.

### 2.2. Data overview and management

Due to the spatial, time-independent nature of the problem, GIS-based datasets must be used in this assessment method. These datasets serve as model inputs and are classified as primary or secondary data based on their origin. Primary data consist of original vector layers or raster files obtained directly from online sources, whereas secondary data are derived from primary data through processing. Table 2 summarizes the datasets required for the model, as well as those available and used in this study, indicating whether they are primary or secondary. The most effective way to generate secondary data from primary sources is to process them using dedicated GIS data management software. In this study, QGIS (an open-source and user-friendly software) was used to enhance the method's replicability [32]. GIS data management was further optimized by developing a dedicated tool within the QGIS modeler, enabling:

- the selection of ineligible areas for offshore wind farms and associated $H_2$ hubs.
- the optimization of the spatial domain by removing ineligible areas.
- the storage of relevant GIS data in a database vector layer, restricted to eligible locations only.

After completing the GIS-based dataset, Microsoft Excel was employed as a complementary tool to streamline calculations and facilitate updates. Excel spreadsheets were also used to define the space-independent techno-economic parameters of the model. Finally, interoperability between QGIS and the.csv files derived from.xlsx files enabled for result rendering and analysis.

### 2.3. Eligibility analysis for domain optimization

Before developing the techno-economic model, a preliminary optimization of the studied spatial domain is required to reduce computational effort and processing time. This optimization must rely on the most commonly used constraints reported in the literature. Such constraints may be established by regional, national, or international regulations or, more frequently, defined arbitrarily by researchers conducting techno-economic evaluations.

For this method, the set of exclusion parameters detailed in Table 3 was selected and recommended also for similar future studies, to ensure that area exclusion is based on the most objective and widely adopted criteria. This approach supports a cautious evaluation of sea eligibility, leaving the application of more socially driven or arbitrarily defined constraints to dedicated spatial planning or site-selection studies. Although this more conservative strategy may require greater computational effort compared with more restrictive approaches, it ensures higher versatility while preserving result reliability, making the outputs suitable for both specific studies (e.g., those mentioned above) and broader energy system model analyses. This is particularly relevant for study areas that have been rarely assessed, such as the northern Adriatic Sea.

**Table 2**
GIS datasets to be used in the model and applied in this case study.

| GIS-data | p*/s** | Primary files name[1] | Primary source[1] | Secondary origins[1] | Format | Raster/Grid resolution |
|---|---|---|---|---|---|---|
| Weibull k (100 m) | p | Grid_nazionale.shp | AEOLIAN [33] | – | Vector | 1.4 km x 1.4 km |
| Mean wind speed (100 m) | p | Grid_nazionale.shp | AEOLIAN [33] | – | Vector | 1.4 km x 1.4 km |
| Oil and gas pipelines | p | OeGpipelines.shp | EMODnet [34] | – | Vector | |
| Oil and gas platforms | p | platform_points.shp | EMODnet [34] | – | Vector | |
| Telecommunication cables lines | p | shomcableLines.shp sigcableLines.shp | EMODnet [34] | – | Vector | |
| Ports | p | portvesselsPoint.shpportgoodsPoint.shp | EMODnet [34] | – | Vector | |
| Protected areas | p | natura2000areas.shp | EMODnet [34] | – | Vector | |
| Route density | p | wid6-cargo-all_europe-yearly-20210101000000_20211231235959-tdm-grid.tif | EMODnet [34] | – | Raster | 1 km x 1 km |
| Ship density | p | 2021_st_All_avg_seatraffic.tif | EMODnet [34] | – | Raster | 1 km x 1 km |
| Bathimetry | p | gebco_2023_n47.0_s39.0_w11.0_e21.0.tif | GEBCO [35] | – | Raster | 0.00416 degrees east x 0.00416 degrees north |
| Weibull parameter A | s | – | – | Grid_nazionale.shp | Vector | 1 km x 1 km |
| Distance to the shore | s | – | – | Grid_nazionale.shp | Vector | 1 km x 1 km |
| Distance to the port | s | – | – | Grid_nazionale.shp; portvesselsPoint.shp andportgoodsPoint.shp | Vector | 1 km x 1 km |
| Land | s | – | – | gebco_2023_n47.0_s39.0_w11.0_e21.0.tif | Vector | |
| Shores | s | – | – | 2021_st_All_avg_seatraffic.tif | Vector | |

[1]for this study; * p = primary; ** s = secondary.

**Table 3**
Exclusion parameters and constraints used in this case study.

| Exclusion parameters | Exclusion rules | Exclusion buffer | Measure Unit | References |
|---|---|---|---|---|
| Bathimetry | <-1000 | None | m a.s.l. | [36,37] |
| Oil and Gas pipelines | excluded | 750 | m (per side) | [38] |
| Oil and Gas platforms | excluded | 2.140 | km | [36] |
| Signal Cables lines | excluded | 500 | m (per side) | [38] |
| Shom Cables lines | excluded | 500 | m (per side) | [38] |
| Land | excluded | None | – | [38] |
| Shores | excluded | 10 | km | [38] |
| Protected areas | excluded | 1 | km | [38,39] |
| Route density (all, year) | >200 | None | routes/km$^2$/year (= ships/km$^2$/year) | [39] |
| Ship density (yearly average) | >200 | None | ships/km$^2$/year | [39] |

### 2.4. System model

Regarding $H_2$ production, and following the findings of previous studies such as [15,19,23] and [17], the system's technical configuration was assumed to follow an offshore centralized layout. Since the model is intended to evaluate maximum $H_2$ producibility and the associated LCOH$^*$, the offshore hub was designed without electrical transmission to the mainland. However, the model structure remains flexible and can be easily extended to include such a connection if required.

The system configuration, shown in Fig. 2, consists of the following three main components:

1. an offshore wind farm (OWF);
2. a hydrogen production plant (H2PP), equipped with a proton exchange membrane electrolyzer (PEMEL) selected as the most suitable technology for this type of application [17];
3. a hydrogen transportation facility, consisting of a dedicated pipeline for delivering hydrogen to the nearest suitable port (i.e., ports capable of supporting for construction and maintenance of OWFs and hydrogen production and delivery hubs).

Each cell within the discretized spatial domain represents this conceptual system, independent of the actual spatial extent of the corresponding system that would be built in reality, with the electrolyzer assumed to be located at the cell centroid (see the case-study schematics in Fig. 2). Therefore, all distance-dependent parameters refer to the cell's centroid position (i.e., the electrolyzer's location). Since the pipeline is included within the system boundaries, its cost is accounted for in the techno-economic model (see Section 2.6.3). Consequently, the LCOH$^*$ resulting from the model and assigned to the cell hosting the H2PP should be interpreted as the cost of hydrogen delivered to the nearest suitable port.

### 2.5. Producibility model

The producibility model was developed with total hydrogen production (THP$^*$) as its final output. However, as shown in Fig. 3 and detailed in Eqs. (15) and (16), THP$^*$ can only be determined after evaluating the annual energy consumed by the PEMEL (AEC$^*$) and the annual hydrogen production (AHP$^*$). The models used for these calculations naturally derive from the one employed for assessing annual energy producibility (AEP$^*$) presented below.

The entire producibility model was developed to analytically evaluate THP$^*$ and the related parameters while balancing reliability and input data availability. It was also designed to remain relatively independent of specific technologies, allowing for straightforward adaptation to different turbine characteristics. For this reason, the wind farm capacity factor (CF) and full load hours (FLH) were excluded as input data. To ensure this flexibility, and considering that empirical turbine power curves are generally easier to find online or in the literature without their power coefficient curve ($C_p(v)$), a reliable approximation of the correct power curve shown in Eq.(2) [17], which avoids the use of $C_p(v)$, is proposed. This approximation, presented in Eq.(3), was formulated using a piece-wise function that models the ramp-up section as a power function of degree l. The values of l and m of Eq.(3) can be obtained from the interpolation of a discretized and normalized $P_T(v)$ (as it had been done in the case study introduced in *Section 2.8*).

$$P_T(v) = \begin{cases} 0 & for \quad v < v_i \\ \frac{\rho_{air} \cdot A_{rotor}}{2} \cdot C_p(v) \cdot v^3 & for \quad v_i \le v < v_r \\ P_{T,nom} & for \quad v_r \le v < v_o \\ 0 & for \quad v \ge v_o \end{cases} \tag{2}$$

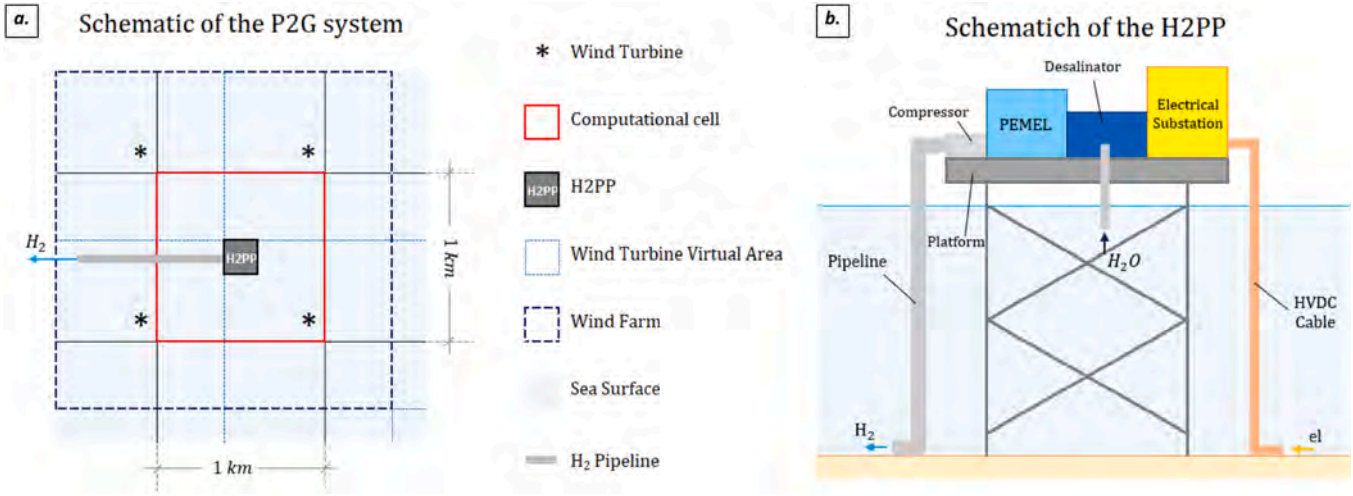


**Fig. 2.** Schematic of the offshore power-to-gas (P2G) system: a. top view of the system with real and computational (i.e., cell) system extension; b. side view of the hydrogen production plant (H2PP).

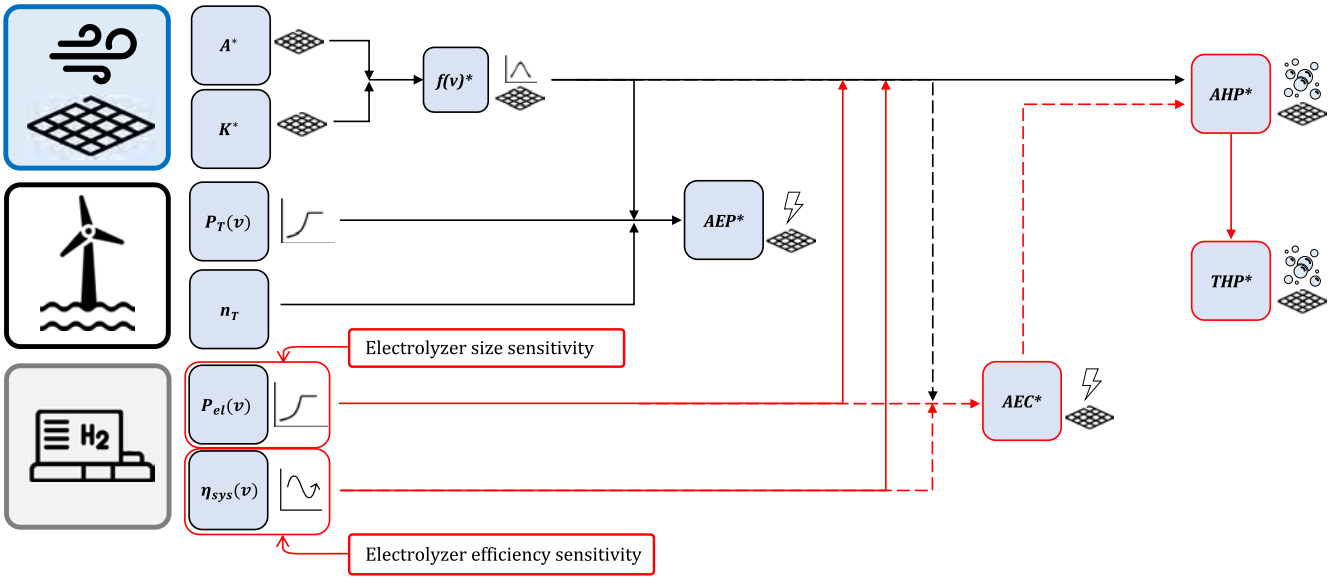


**Fig. 3.** Schematic of the producibility model. Red lines and red- bordered boxes indicate the steps involved in the sensitivity analyses. Looking at the solid lines, these steps correspond to the evaluation of the spatially resolved Annual Hydrogen Production ($AHP^*$) and spatially resolved Total Hydrogen Production ($THP^*$), based on the electrolyzer's power and efficiency values assumed for the sensitivity analyses. Alternatively, following the dashed lines, when $\eta_{sys}(v)$ is a constant value the model simplifies, allowing an easy estimation of $AHP^*$ via the spatially solved Annual Hydrogen Consumption ($AEC^*$).

$$P_T(v) \simeq \begin{cases} 0 & for \quad v < v_i \\ P_{T,nom} \cdot (m \cdot v^l) & for \quad v_i \le v < v_r \\ P_{T,nom} & for \quad v_r \le v < v_o \\ 0 & for \quad v \ge v_o \end{cases} \tag{3}$$

where $P_{T,\ nom}$ is the nominal power of the wind turbine and $v_i$, $v_o$ and $v_r$ are the cut-in, cut-off and the rated wind speeds, respectively. The approximated piecewise function for $P_T(v)$ enables the analytical evaluation of $AEP^*$, $AEC^*$ and $AHP^*$. Assuming that at least one of the 2 parameters of the Weibull probability density function $f(v)^*$ is available (i.e., the shape factor $k^*$ and the scale factor $A^*$), along with the site mean velocity $v_m^*$ for each point of the domain, the evaluation of the $AEP^*$ [kt/y] is given by Eq. (4):

$$\begin{aligned} AEP^* &= 8760 \cdot n_T \cdot \int_{v_i}^{v_o} (f(v)^* \cdot P_T(v))\,dv \\ &= 8760 \cdot n_T \cdot P_{T,nom} \cdot \left[ \int_{v_i}^{v_r} (f(v)^* \cdot m \cdot v^l)\,dv + \int_{v_r}^{v_o} f(v)^*\,dv \right] \end{aligned} \tag{4}$$

where $n_T$ is the number of turbines per farm and 8760 are the hours per year. Using the explicit form of the Weibull probability density function $f(v)^*$, which is reported in Eq. (5), and the definition of upper incomplete gamma function reported in Eq. (6):

$$f(v)^* = \frac{k^*}{A^*} \cdot \left(\frac{v}{A^*}\right)^{k^*-1} e^{\left[-\left(\frac{v}{A^*}\right)^{k^*}\right]} \tag{5}$$

$$\Gamma(x,s) = \int_x^{\infty} (t^{s-1}\ e^{-t})\,dt \tag{6}$$

the analytical solution of $AEP^*$ can be rearranged as:

$$\begin{aligned} AEP^* = 8760 \cdot n_T \cdot P_{T,nom} \cdot \Bigg[ & m \cdot A^{*l} \cdot \left[ \Gamma\left( \left(\frac{v_i}{A^*}\right)^{k^*}, \frac{k^*+1}{k^*} \right) \right. \\ & \left. - \Gamma\left( \left(\frac{v_r}{A^*}\right)^{k^*}, \frac{k^*+1}{k^*} \right) \right] + e^{\left[-\left(\frac{v_r}{A^*}\right)^{k^*}\right]} - e^{\left[-\left(\frac{v_o}{A^*}\right)^{k^*}\right]} \Bigg] \end{aligned} \tag{7}$$

As a first approach, the size of the electrolyzer was assumed to be equal to the maximum capacity of the wind farm, ensuring that all the available energy produced by the off-grid wind farm is used, as defined in Eq. (8). Therefore, the power absorption curve of the electrolyzer as a function of wind speed is represented by $P_{el}(v)$ (see Fig. 5):

$$P_{el,nom} = n_T \cdot P_{T,nom} \quad \text{and} \quad v_{r,el} = v_r \tag{8}$$

$$P_{el}(v) \simeq \begin{cases} 0 & for \quad v < v_i \\ P_{el,nom} \cdot (m \cdot v^l) & for \quad v_i \le v < v_{r,el} \\ P_{el,nom} & for \quad v_{r,el} \le v < v_o \\ 0 & for \quad v \ge v_o \end{cases} \tag{9}$$

where $P_{el,nom}$ is the nominal power of the electrolyzer and $v_{r,el}$ is the rated wind speed above which the electrolyzer can absorb its nominal power $P_{el,nom}$. This implies that for a given wind speed, all the energy produced by the wind farm will be directly used as input energy for the electrolyzer. Therefore, the $AEC^*$ can be evaluated in the same way as the $AEP^*$ with the only substitution of $n_T \cdot P_{T,nom}$ with $P_{el,nom}$ (i.e., the maximum power that the electrolyzer can exploit):

$$AEC^* = 8760 \cdot \left[ \int_{v_i}^{v_{r,el}} (f(v)^* \cdot P_{el}(v))\,dv + \int_{v_{r,el}}^{v_o} (f(v)^* \cdot P_{el,nom})\,dv \right] \tag{10}$$

$$\begin{aligned} AEC^* = 8760 \cdot P_{el,nom} \Bigg[ & m \cdot A^{*l} \cdot \left[ \Gamma\left( \left(\frac{v_i}{A^*}\right)^{k^*}, \frac{k^*+1}{k^*} \right) \right. \\ & \left. - \Gamma\left( \left(\frac{v_{r,el}}{A^*}\right)^{k^*}, \frac{k^*+1}{k^*} \right) \right] + e^{\left[-\left(\frac{v_{r,el}}{A^*}\right)^{k^*}\right]} - e^{\left[-\left(\frac{v_o}{A^*}\right)^{k^*}\right]} \Bigg] \end{aligned} \tag{11}$$

By defining the specific energy consumption of the hydrogen production plant (H2PP) and electrolyzer as given in Eqs. (12) and (13) (respectively SEC and $SEC_{el}$), the $AHP^*$ is determined similarly to the $AEC^*$ using Eq. (14):

$$SEC(P_{el}(v)) = SEC_{el}(P_{el}(v)) + SEC_{comp} + SEC_{des} \tag{12}$$

$$SEC_{el}(P_{el}(v)) = \frac{LHV_{H_2}}{\eta_{el}(P_{el}(v))} \tag{13}$$

$$AHP^* = 8760 \cdot \left[ \int_{v_i}^{v_{r,el}} \left( f(v)^* \cdot \frac{P_{el}(v)}{SEC(v)} \right) dv + \int_{v_{r,el}}^{v_o} \left( f(v)^* \cdot \frac{P_{el,nom}}{SEC_{nom}} \right) dv \right] \tag{14}$$

where $SEC_{comp}$ is the specific energy consumption of the compressor, $SEC_{des}$ is the specific energy consumption of the desalination plant, $\eta_{el}(P_{el}(v))$ is the lower heating value (LHV) efficiency of the PEMEL system and $LHV_{H_2}$ is the hydrogen lower heating value. It should be noted that the assumed value of $\eta_{el}$ (and consequently $SEC_{el}$) already includes the energy consumption associated with the electrolyzer's balance of plant. Since the PEMEL efficiency depends on the PEMEL power function, it can be expressed as a piecewise function directly dependent on the wind speed ($\eta_{el}(v)$). This function exhibits variable behavior within the speed range corresponding to the ramp-up phase of the $P_T(v)$ curve, and a constant behavior in the speed range where the wind turbine operates at its nominal power $P_{T,nom}$. As it depends on $\eta_{el}(v)$, the same holds for $SEC_{el}(P_{el}(v))$, which can be expressed as a piecewise function of the wind speed, denoted as $SEC_{el}(v)$. The generic function of the total H2PP specific energy consumption SEC(v) inherits such a dependency from v. Accordingly, $SEC_{el}(P_{el}(v))$ evaluated in $P_{el,nom}$ is referred to as $SEC_{el,nom}$ and is used to define the corresponding value of the entire H2PP specific energy consumption with the electrolyzer working at its nominal conditions $SEC_{nom}$.

In this work, the impact of $\eta_{el}(v)$ on producibility is investigated by comparing different design approaches. To achieve this, two distinct scenarios were considered:

1. Approximation of the PEMEL efficiency as a constant value, using $\eta_{el,ave}$, the average value of $\eta_{el}(v)$, or $\eta_{el,nom}$, the PEMEL system efficiency value under nominal conditions ($\eta_{el}(P_{el,\,nom})$);
2. Detailed modeling of the PEMEL efficiency, representing $\eta_{el}(v)$ as an empirical analytical function of the wind speed.

While the second scenario allows for the development of the method for the most general case (see Eq.(14)), the former simplifies Eq. (14) into Eq. (15), allowing for the direct use of $AEC^*$ to evaluate $AHP^*$:

$$AHP^* = 8760 \cdot \frac{1}{SEC_{nom}} \left[ \int_{v_i}^{v_{r,el}} (f(v)^* \cdot P_{el}(v))\, dv + \int_{v_{r,el}}^{v_o} (f(v)^* \cdot P_{el,nom})\, dv \right] = \frac{AEC^*}{SEC_{nom}} \tag{15}$$

When $\eta_{el}(v)$ is approximated using $\eta_{el,ave}$, the term $SEC_{nom}$ in Eq.(15) must be replaced with $SEC_{ave}$, which is the average value of SEC(v) over the wind speed domain. The detailed specific energy consumption functions adopted for the case study analyzed in this article are presented and referenced in *Section 2.8*. Finally, the $THP^*$ can be evaluated by the discounted sum of $AHP^*$ over the entire project lifetime:

$$THP^* = AHP^* \cdot \Sigma_{t_i=0}^{t_{life}-1} \frac{1}{(1+r)^{t_i}} \tag{16}$$

where $t_{life}$ is the lifetime of the system (i.e., the lifetime of the wind farm), $t_i$ is the $i^{th}$ operational year and r is the discount rate.

### 2.6. Economic models

This section presents the cost structures and the main cost components for the various elements of the P2G system. For the sake of brevity, only the most relevant equations of the model will be presented here, while a comprehensive description of the other assumptions adopted for the construction of the economic model is provided in the *Supplementary Material*. The overall framework for evaluating the main cost components is summarized in Fig. 4.

#### 2.6.1. Offshore wind farm

The composition of the wind farm's capital expenditures ($CAPEX^*_{WF}$) is described in Eq. (17)

$$CAPEX^*_{WF} = C^*_F + C^*_T + C_{AC} + C_{ss} + C_{D\&C} \tag{17}$$

where $C^*_F$ represents the cost of the foundations, $C^*_T$ is the cost of the turbines, $C_{AC}$ refers to the cost of the array cables connecting the wind farm turbines, $C_{ss}$ is the cost of the electrical substation and $C_{D\&C}$ is the cost of development and consenting. Following the examples encountered in the reviewed literature, the specific costs used to estimate the $CAPEX^*_{WF}$ were expressed in millions of euros (M€) per megawatt (MW) of installed OWF and are listed in *Supplementary Material Table S.1*, with all other parameters required from the OWF economic model. As this study focuses on the spatial dependency of the results, only the spatially dependent parameters influencing $CAPEX^*_{WF}$ are described in the following section [17]. The composition of the foundation costs is given by Eq. (18):

$$C^*_F = F_{man,f} + F^*_{trans} + F_{install} \tag{18}$$

where $F^*_{trans}$ is the transportation cost of the foundations to the offshore installation site, $F_{install}$ is their installation cost and $F_{man,\,f}$ is their manufacturing cost (the latter two were assumed to be spatially independent). The transportation cost depends on the substructure transportation cost $f^*_{trans}$ and, in the case of floating OWF, on the transportation cost for the moorings $M^*_{trans}$, which consists of both the anchors transportation cost ($An^*_{trans}$) and lines transportation cost ($L^*_{trans}$). Eqs. (19)-(23) further define all these parameters:

$$F^*_{trans} = f^*_{trans} + M^*_{trans} \tag{19}$$

$$M^*_{trans} = \begin{cases} 0 & for \quad bottom-based \quad OWF \\ An^*_{trans} + L^*_{trans} & for \quad floating \quad OWF \end{cases} \tag{20}$$

$$An^*_{trans} = t^*_{2s} \cdot \frac{v_{ves}}{v_{M,an,ves}} \cdot \frac{n_{m,f} \cdot n_{an,m}}{n_{an,trip}} \cdot c_{M,an,ves} \cdot n_T \tag{21}$$

$$L^*_{trans} = t^*_{2s} \cdot \frac{v_{ves}}{v_{M,l,ves}} \cdot \frac{n_{m,f} \cdot n_{l,m}}{n_{l,trip}} \cdot c_{M,l,ves} \cdot n_T \tag{22}$$

$$f^*_{trans} = \frac{t^*_{2s}}{n_{f,trip}} \cdot c_{f,ves} \cdot n_T \tag{23}$$

where $v_{ves}$ is the general vessel speed, $n_{m,f}$ is the number of moorings per floating platform, $n_{an,m}$ is the number of anchors per mooring (here assumed 1), $n_{l,m}$ is the number of lines per mooring (here assumed 1), $n_{an,trip}$ is the number of anchors that can be transported per trip by a vessel, $v_{M,an,ves}$ and $v_{M,l,ves}$ are the speeds of towing for vessels carrying anchors and lines, $c_{M,an,ves}$ and $c_{M,l,ves}$ are the daily specific costs for renting the vessel for the anchors and lines transportation, $n_{f,trip}$ is the number of foundations (floating platforms without the mooring system M) transported per trip, $c_{f,ves}$ is the rental cost of the vessel transporting the foundations, $n_T$ is the number of turbines per wind farm and $t^*_{2s}$ is the trip time of the vessels from the harbor to the installation site and back (see Eq. (24)).

$$t^*_{2s} = 2 \cdot \frac{D^*_p}{v_{ves} \cdot h_{working,day}} \tag{24}$$

The spatial dependency of all these cost components, as well as those representing the contribution of the wind turbines (see Eq. (26)), is

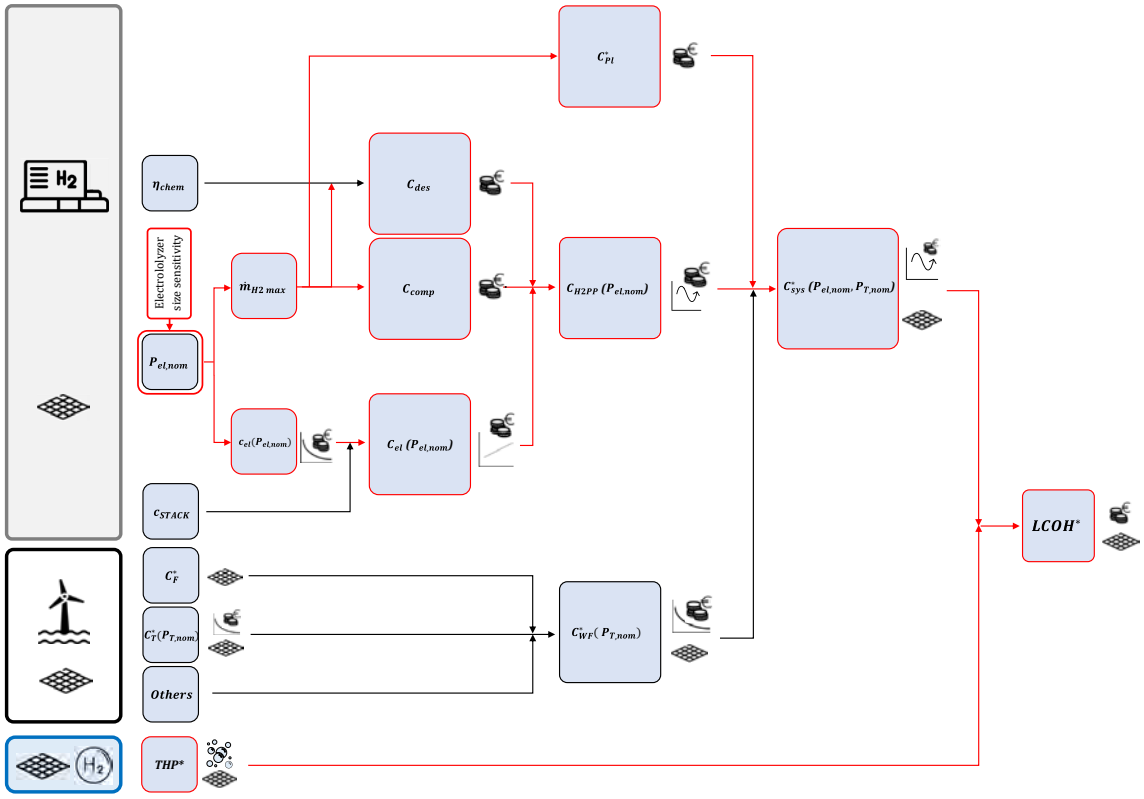


**Fig. 4.** Structure of the economic model for the LCOH assessment (red lines and red bounded boxes indicate the steps involved in the sensitivity analyses), where $C^*_{sys}(P_{el,nom}, P_{T,nom})$ is the total actualized cost of the entire P2G system, $C^*_{WF}(P_{t,nom})$ is the cost of the entire OWF, $c_{STACK}$ is the specific cost of the stack replacement.

primarily attributed to $t^*_{2s}$, where $D^*_p$ is the distance evaluated from the installation point (assumed to be the centroid of each cell in the model) to the nearest harbor suitable for OWF manufacturing and maintenance activities, and $h_{working,day}$ denotes the number of working hours per day.

The only other spatially dependent component of $CAPEX^*_{WF}$ is $C^*_T$ (turbine transportation cost) as described in Eqs. (25) and (26):

$$C^*_T = T_{man} + T^*_{trans} + T_{install} \tag{25}$$

$$T^*_{trans} = \frac{t^*_{2p}}{n_{T,trip}} \cdot c_{T,ves} \cdot n_T \tag{26}$$

where $T_{man}$, $T^*_{trans}$ and $T_{install}$ are, respectively, the turbine manufacturing, transportation and installation costs while $n_{T,trip}$ is the number of trips to transport an entire turbine and $c_{T,ves}$ is the specific cost for the turbine transportation vessel.

### 2.6.2. Offshore hydrogen production plant

The offshore H2PP is the offshore hub for the hydrogen production, consisting of: a desalination plant for producing deionized water to supply the electrolyzer; a PEMEL used for the hydrogen production; a compression unit to transport the produced hydrogen to the delivery point and the offshore platform, which houses all hub facilities along with the electrical substation of the OWF. Accordingly, the capital expenditure of the H2PP was defined as follows:

$$CAPEX_{H2PP} = C_{des} + C_{el} + C_{comp} + C_{plat} \tag{27}$$

where $C_{des}$, $C_{el}$, $C_{comp}$ and $C_{plat}$ are the costs of the desalination plant, the electrolyzer, the compression and the offshore platform, respectively. In this study, the cost of the platform was considered as that of a bottom-fixed structure, due to the lack of available data in the literature for floating platforms in deep-water environments. All specific costs used for the evaluation of the $CAPEX_{H2PP}$, as well as the other relevant parameters used for its evaluation, are listed in the *Supplementary Material (Table S.2)*. Notably, the specific costs of the H2PP are expressed for MW of installed electrolyzer capacity. As evident from Eq. (27), the $CAPEX_{H2PP}$ has been assumed to be spatially independent. This assumption is justified by the results from the sensitivity analysis on electrolyzer sizing, presented in *Section 3.6*.

The compressor capacity was determined by Eq. (28), while the normalized capacity of the desalination plant (rarely considered in such studies) was modeled using Eq. (29)

$$P_{comp} = \dot{m}_{H_2\,max} \cdot \frac{R \cdot T \cdot Z}{\eta_{comp} \cdot M_{H_2}} \cdot \frac{N \cdot \gamma}{\gamma - 1} \cdot \left[ \left( \frac{p_o}{p_i} \right)^{\frac{\gamma-1}{N \cdot \gamma}} - 1 \right] \tag{28}$$

$$\dot{v}_{H_2O\,power} = \eta_{chem} \cdot \dot{m}_{H_2\,power} \cdot 3600 \tag{29}$$

where $\dot{m}_{H_2\,max}$ is the maximum hydrogen mass flow rate, R is the ideal gas constant, T is the temperature, Z is the compressibility factor, $\eta_{comp}$ is the efficiency of compression, $M_{H_2}$ is the molecular mass of $H_2$, N is the number of compression stages, $\gamma$ is the isentropic coefficient, $p_o$ and $p_i$ are the outlet and inlet pressures, $\dot{v}_{H_2O\,power}$ is the volumetric flowrate of water required by an electrolyzer of 1MW to produce $\dot{m}_{H_2 power}$ (i.e., its production rate) and $\eta_{chem}$ is the chemical efficiency of conversion of feed water into the hydrogen in output. Both the compressor and the desalination plant capacities were derived based on the design variable $P_{el,nom}$ from which derives $\dot{m}_{H_2\,max}$. The specific values assumed for all these parameters in the demonstrative case study concerning the northern Adriatic Sea are detailed in *Section 2.8* and *Tables S.1 and S.2* of the *Supplementary Material*.

While the OPEX of the other costs are evaluated as a percentage of CAPEX or through a fixed specific operational annual cost actualized for each operational year, the $OPEX_{H2PP}$ had to account also for the electrolyzer stack replacement as its lifetime $t_{stack}$ is typically shorter than

that of the entire system. Consequently, $OPEX_{H2PP}$ was evaluated as reported in Eq. (30)

$$OPEX_{H2PP} = \sum_{t_i=0}^{t_{life}-1} \frac{(OPEX_{des} + OPEX_{el} + OPEX_{comp} + OPEX_{plat} + OPEX_{stack,t_i})}{(1+r)^{t_i}} \quad (30)$$

where $t_{life}$ is the system lifetime, $r$ is the discount rate, $t_i$ is the $i^{th}$ operational year, and $OPEX_{des}$, $OPEX_{el}$, $OPEX_{comp}$, $OPEX_{plat}$, $OPEX_{stack}$ are respectively the desalination plant, PEMEL, compressor, platform and stack OPEXs. The value of $OPEX_{stack}$ is assumed to be zero in all years except during replacement years (see the *Supplementary Material, Section 1.2*).

### 2.6.3. Pipeline

The model for the evaluation of the pipeline CAPEX (i.e., $CAPEX^*_{pl}$), reported in Eq. (31), was designed to adapt the capacity of the pipeline to the hydrogen flowrate production in nominal conditions of the electrolyzer:

$$CAPEX^*_{pl} = 2 \cdot \left( 16 \cdot 10^3 \frac{P_{el,nom} \cdot \dot{m}_{H_2\ power}}{\rho_{H_2} \cdot \nu_{H_2} \cdot \pi} + 1197.2 \sqrt{\frac{P_{el,nom} \cdot \dot{m}_{H_2\ power}}{\rho_{H_2} \cdot \nu_{H_2} \cdot \pi}} + 329 \right) \cdot \frac{D^*_{injec}}{10^3} \quad (31)$$

where $\nu_{H_2}$ and $\rho_{H_2}$ are the mean velocity and the density of the $H_2$ in the pipe, respectively. $D^*_{injec}$ is the minimum distance of the offshore site from the injection point in the mainland or to an existing gas pipeline that could be retrofitted for hydrogen transport. Being this equation based on [17], the monetary coefficients of Eq.(31) were updated from $€_{2023}$ to $€_{2024}$ (see *Supplementary Material, Section 1.3* [40]) and divided by a $10^3$ factor to give results in [M€] instead of [k€].

## 2.7. Size ratio sensitivity analysis

According to [20,21] and [41], a relationship exists between the LCOH and the optimal ratio between the electrolyzer size and the nominal wind farm capacity ($WF_c$). To investigate this relationship, a sensitivity analysis was conducted to identify the optimal size of the PEMEL (and thus of the whole H2PP, whose size and costs depend on the value of $P_{el,nom}$) with respect to the $WF_c$. The independent variable of the sensitivity analysis was the electrolyzer size ratio $SR_{el}$, as defined in Eq. (32), which was evaluated for different $j^{th}$ electrolyzer sizes ($P_{el,nom,j}$) gradually decreasing from the value of the $WF_c$ until its 2 %. The $WF_c$ was kept constant across the sensitivity analysis.

$$SR_{el,j} = \frac{P_{el,nom,j}}{WF_c} \quad (32)$$

Even though the sensitivity analysis was performed over the entire spatial domain, a set of characteristic locations were identified based on their specific relevance to verify the consistency of the results across the studied domain. These locations were chosen to represent the limit boundaries of the multivariable techno-economic domain (i.e., location with best and worst techno-economic input variables). The set of variables considered to identify these locations were: distance to port ($D^*_p$), depth ($d^*$) and capacity factor ($CF^*$). According to the presented model, a new $P_{el,j}(v)$ had to be designed for each tested $SR_{el,j}$ to evaluate the updated hydrogen producibility. This was done by identifying the updated $v_{r,el,j}$, which is the rated velocity at which the total power produced by the OWF ($P_{WF}(v)$) reaches the $P_{el,nom,j}$ chosen for the $j^{th}$ simulation of the sensitivity analysis. An example of $P_{el,j}(v)$ for $SR_{el,j}$ equal to 0.5 and 1 has been reported in Fig. 5. The $v_{r,el,j}$ has been evaluated for each step of the sensitivity analysis according to Eq. (33):

$$v_{r,el,j} = \left( \frac{P_{el,nom,j}}{m} \right)^{\frac{1}{l}} \quad (33)$$

## 2.8. Case study and input data

To demonstrate the reliability of the presented method and to identify the optimal value of $SR_{el}$, a case study was carried out over the spatial domain of the Northern Adriatic Sea. The extent of the studied area is defined in the EPSG:3035 LAEA Europe coordinate reference system: North 2,261,837 to 2,513,837 m; East 4,503,968 to 4,740,968 m, with a 1 $km^2$ resolution. The wind distribution is illustrated in Fig. 6, represented by the Weibull probability density function parameters defined in Eq. (5), namely $k^*$ and $A^*$.

Since the analysis was not demand-driven, the OWF configuration could be chosen arbitrarily. Therefore, a 20 MW OWF consisting of four standard "NREL_5MW_126_RWT" [42] turbines were used for the simulation (the main technical parameters reported in Table 4). To neglect wake losses, minimum axial and lateral inter-turbine free distances of 7 and 5 rotor diameters (D), respectively, were applied [20]. This resulted in an installed power density of 5 MW per cell (i.e., 1 turbine per cell), with the real OWF layout depicted in Fig. 2.

While it is well known that port characteristics such as (minimum draft, berth or throughput class, hazardous-cargo handling, shore-side hydrogen readiness) determine their suitability as construction and maintenance hubs for offshore systems, this study imposed no constraints other than restricting the analysis to commercial harbors. This choice was motivated by the absence of OWFs and offshore hydrogen production facilities in the studied domain, implying that port infrastructure would require adaptation regardless of the reference harbor selected. Consequently, all commercial harbors were assumed to be potentially eligible. Another assumption is that the value associated to the spatial parameter $D^*_p$ is always considered as the Cartesian distance following a least-cost seabed path approach, which is considered reasonable for such high-level studies. The value of $D^*_{inject}$ was set equal to $D^*_p$ in all cases except when assessing the impact of the possible use of an already existing pipeline landing in Croatia, near Pula, for $H_2$ transport. In that case, the potential cost benefit of using an existing pipeline was assessed to determine whether the resulting reduction in transportation costs could justify its inclusion in future, more detailed techno-economic feasibility studies. To this end, the assessment first focused on a preliminary evaluation, aiming to estimate the extreme boundaries of potential LCOH improvement (i.e., the lowest attainable values), while neglecting retrofitting costs (zero retrofitting cost scenario) and considering only those associated with newly built pipeline segments connecting to the existing infrastructure. According to the conclusions reported by [43], these assumptions are realistic when considering natural gas–hydrogen blends in transportation pipelines with a volumetric hydrogen share below 10 % and operating pressures above 16 bar, for which no need of substantial modifications to the existing infrastructure is expected. Alternatively, to obtain more

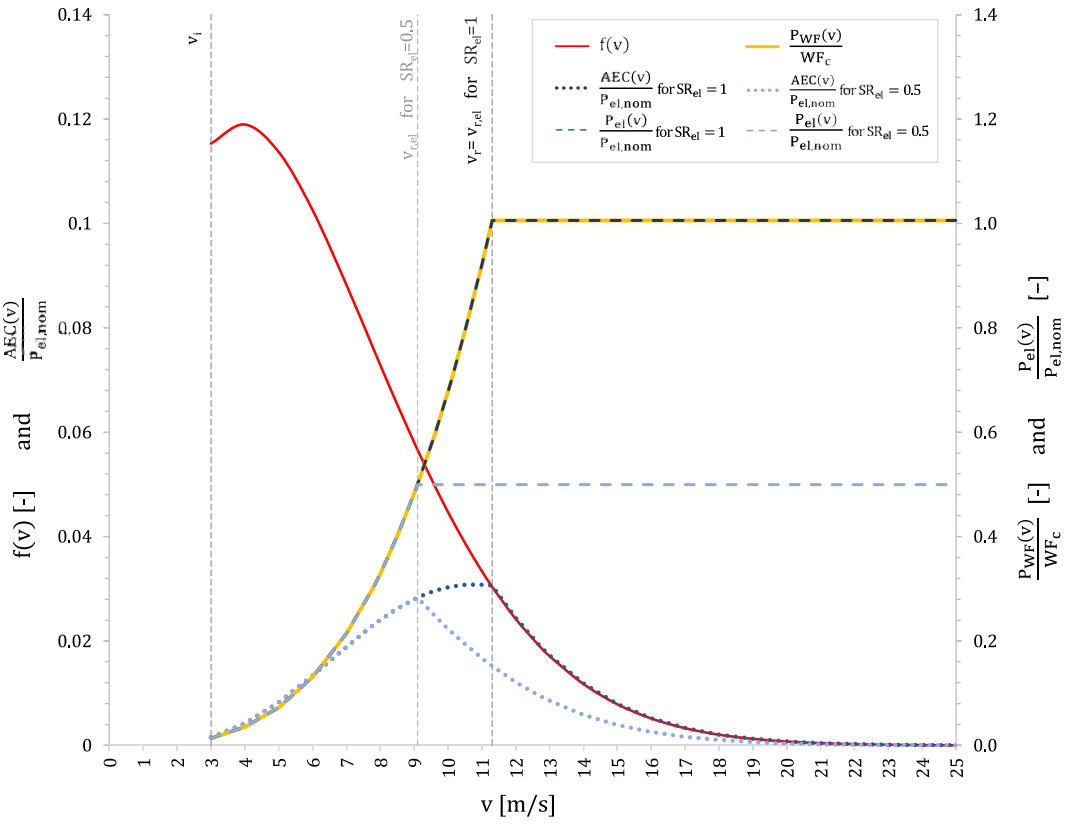


**Fig. 5.** Main curves used in producibility model for a given site: Weibull probability density function for a general site (red curve); Normalized PEMEL input power (dashed curves) for $SR_{el}$ equal to 0.5 and 1; Wind farm power curve $P_{WF}(v) = n_T \cdot P_T(v)$ normalized to the wind farm nominal capacity $WF_c$ (yellow curve); Normalized annual energy consumption curves (dotted curves) for $SR_{el}$ equal to 0.5 and 1 (the area under these curves represents the normalized AEC for the general site).

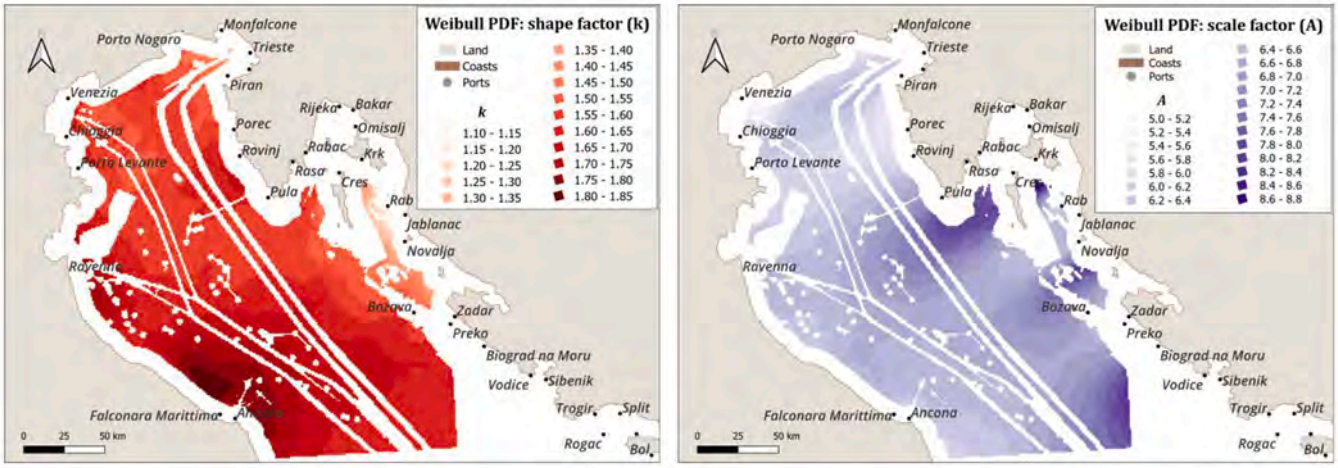


**Fig. 6.** Maps of the parameters of the Weibull probability density function (DFT) across the analyzed domain: $k^*$ (left), $A^*$ (right).

detailed estimates for the transport of pure $H_2$ rather than natural gas–$H_2$ blends, additional costs associated with new materials and complex retrofitting operations (e.g., compressors and valves substitutions, and internal pipe lining and/or material change to prevent embrittlement [44,45]) should be included. To provide a high-level sensitivity analysis of retrofitting-costs impacts, two scenarios were examined: a medium-cost scenario (10 % of the cost of an equivalent new-built hydrogen pipeline [46]), and high-cost scenario (0.546 M€/km [15]). In all these three retrofitting scenarios (zero, medium, and high), locations were considered connected to the existing pipeline only if they were closer to the pipeline than to the nearest port (i.e., if the minimum Cartesian distance between the site and the existing pipeline was shorter than $D_p^*$) and if such a connection yielded an economic benefit, (i.e., the LCOH obtained via the pipelines connection was lower than the LCOH associated with the direct connection to the port). Therefore, for these locations, $D_{inject}^*$ was always set as equal to the minimum Cartesian distance site-existing pipeline.

A size-dependent function for the specific CAPEX of PEM electrolyzers, $c_{el}$ [in M€/MW], was used to conduct a sensitivity analysis on

**Table 4**
Parameters of the wind turbine and the OWF considered for the selected case study.

| Parameter | Value | Unit of measurement |
|---|---|---|
| Turbine | | |
| $P_{T,nom}$ | 5 | MW |
| D | 126 | m |
| Hub height | 90 | m |
| $v_i$ | 3 | m/s |
| $v_r$ | 11.4 | m/s |
| $v_o$ | 25 | m/s |
| Interpolated ramp-up curve parameters | | |
| M | 0.0004 | – |
| L | 3.2291 | – |
| $v_r$ | 11.3 | m/s |
| Offshore Wind Farm | | |
| $n_t$ | 4 | – |
| $WF_c$ | 20 | MW |
| $t_{life}$ | 25 | years |

$SR_{el,j}$. Additionally, to be involved in the design of the SEC(v) analytical function, $\eta_{el}$ requires an expression as a function of the wind speed velocity ($\eta_{el}(v)$). These functions were designed for this case study as reported in Eqs. (34) [47] and (35) [41].

$$c_{el} = \left(g_0 + \frac{g}{P_{el,nom}} P_{el,nom}^{\alpha}\right) \cdot \left(\frac{Y}{Y_0}\right)^{\beta} \cdot cc_{\$2€} \cdot 10^{-3} \quad (34)$$

Here, α is a scaling factor, β is a learning factor, g and $g_0$ are fitting parameters, Y is the installation year (2024), and $Y_0$ (2020) is the reference year as defined in [47]. The term $cc_{\$2€}$ accounts for USD-EUR currency conversion. The function, shown in Fig. 7, was multiplied by $10^{-3}$ to express the specific cost in [M€/MW].

The equation for $\eta_{el}(v)$ reported in Eq. (*35*), whose values already include the balance of plant consumption, was derived from an experimental formulation of $\eta_{el}(P_{el})$:

$$\eta_{el}(v) = \begin{cases} 0 & for \quad v < v_i \\ a \cdot e^{H \cdot v^l} + c \cdot e^{G \cdot v^l} & for \quad v_i \le v < v_{r,el} \\ \eta_{el}\left(v_{r,el}\right) & for \quad v_{r,el} \le v < v_o \\ 0 & for \quad v \ge v_o \end{cases} \quad (35)$$

where l is the exponent used in Eq. (9), and H and G are exponents obtained from experimental data used to construct the efficiency curve in [41]. $\eta_{el}(v_{r,el})$ denotes the efficiency at the electrolyzer rated wind speed. The resulting $\eta_{el}(v)$ and associated $SEC_{el}(v)$ curves are shown in Fig. 7.

For the application considered in this study (hydrogen production and injection into a dedicated pipeline), seawater reverse osmosis (SWRO) is typically assumed for the desalination unit ([48,18]) and both types of centrifugal and reciprocating compressors are permitted by the literature [49]. The specific energy consumptions of the desalination plant ($SEC_{des}$) and compressor ($SEC_{comp}$) for this study were derived from [18] and [17] and set to 0.060 $kWh/kg_{H_2}$ and 0.374 $kWh/kg_{H_2}$, respectively. Specifically, $SEC_{comp}$ represents the energy required to compress hydrogen from the PEMEL outlet pressure (inlet for the compressor) of 30 bar ($p_i$) to 60 bar ($p_o$) for delivery into the gas pipeline.

All techno-economic, space-independent parameters related to the wind turbine and the OWF used in this study are reported in Table 4. The OWP service life, assumed following [17], was extended to represent the operational lifetime of the entire P2G system and is therefore denoted in Table 4 as $t_{life}$. All other techno-economic, space independent parameters are listed and defined in the *Supplementary Material* (particularly *Tables S.1 and S.2*).

As explained in *Section 2.7*, the results of the sensitivity analysis on $SR_{el}$ were represented only for a selected number of sites within the spatial domain. These sites were identified a priori by combining a set of spatially dependent parameters to capture the domain's heterogeneity. By overlying the layers representing the spatial parameters $d^*$ (depth), $D_p^*$ (distance to port) and $CF^*$ (wind farm capacity factor), distinct regions within the domain were identified. In Fig. 8, these regions are color-coded and denoted by capital letters, each letter corresponding to a unique combination of parameters values. Each region was selected because it exhibited an extreme value in one of the three parameters, while the other two remained at average values. This approach enabled the sensitivity analysis to compare locations where a certain parameter exerted a stronger influence on $LCOH^*$ than the others. Consequently, the selected zones include:

- scenarios with average $d^*$ and $CF^*$ values and either deep or shallow waters (blue and light blue areas labelled by A and B, respectively, in Fig. 8);
- scenarios with average $D_p^*$ and $CF^*$ values and either proximity to or distance from ports (orange and pink areas labelled by C and D, respectively, in Fig. 8);

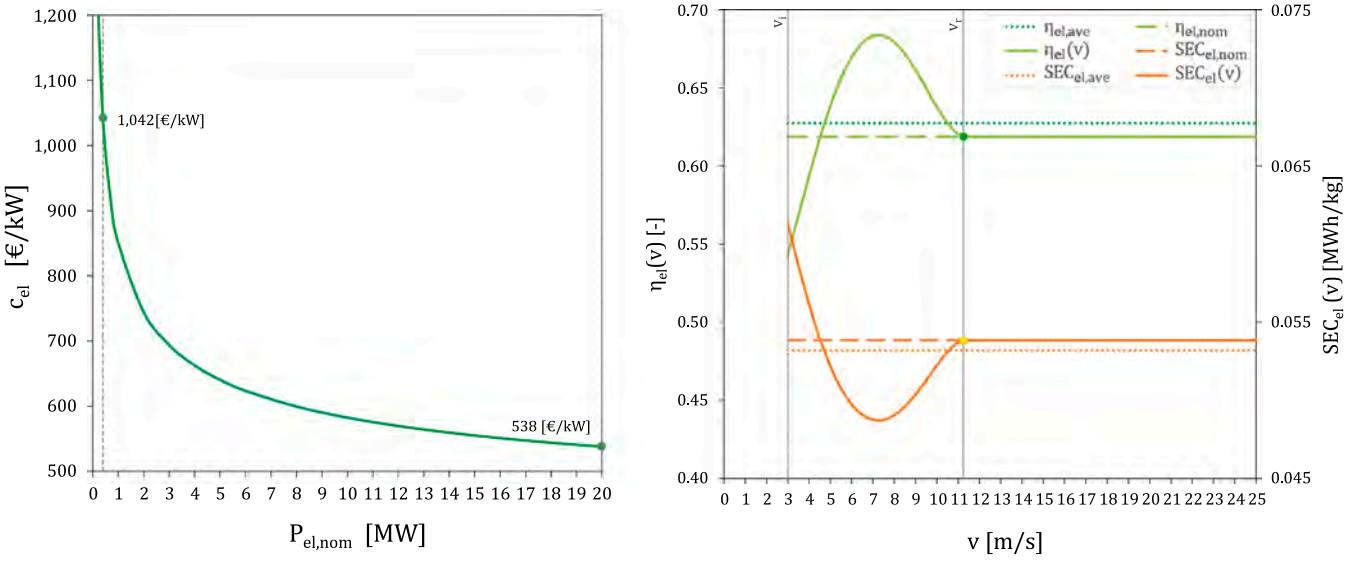


**Fig. 7.** Curve for the specific PEMEL cost as derived from [47] (left); $\eta_{el}(v)$ and $SEC_{el}(v)$ curves as derived from [41] (right).

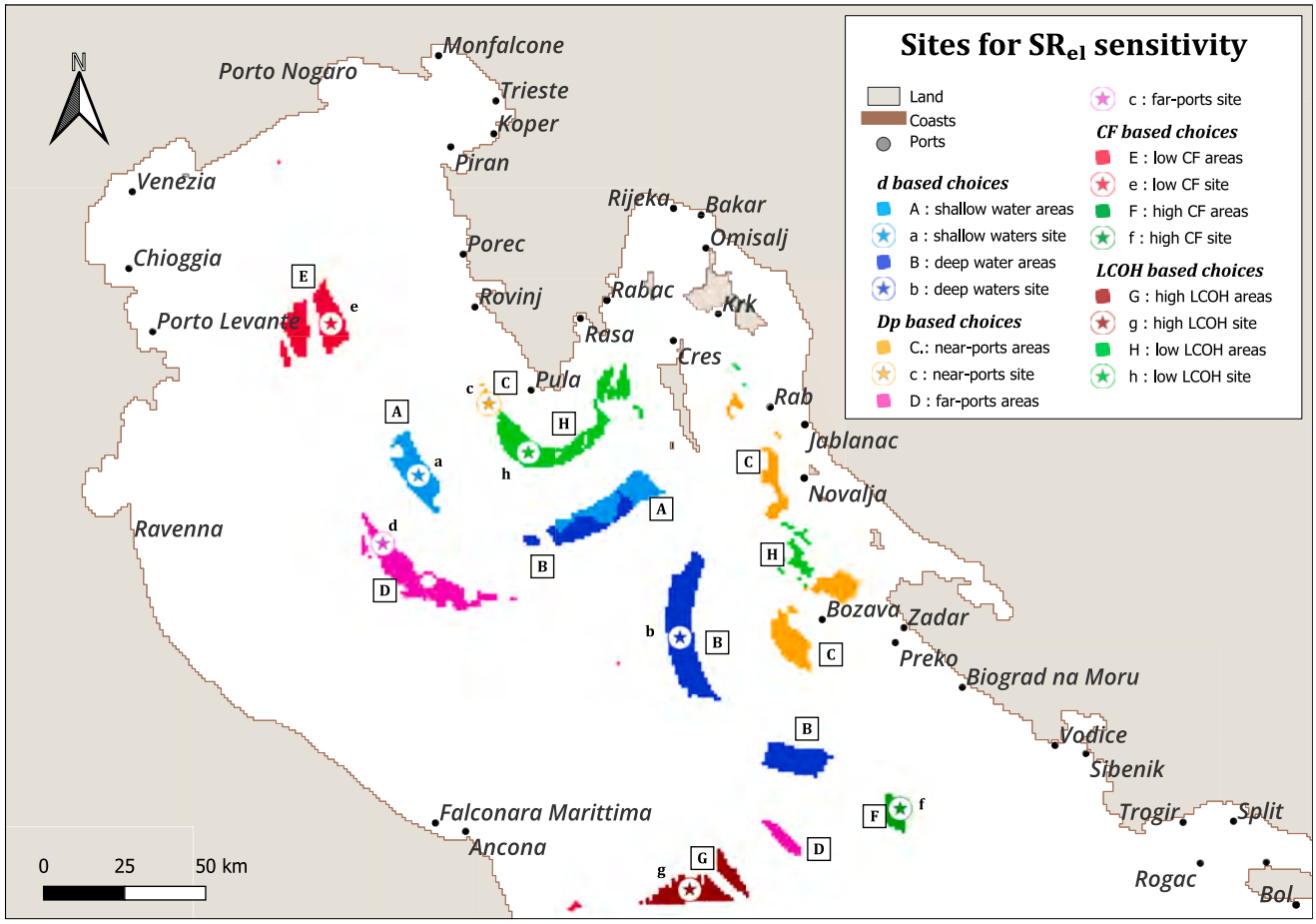


**Fig. 8.** Areas and locations identified to display the $SR_{el}$ sensitivity analysis.

- and scenarios with average $D_p^*$ and $d^*$ values and either high or low $CF^*$ (green and red areas labelled by F and E, respectively, in Fig. 8).

After the $LCOH^*$ assessment, two additional regions were selected to represent the best- and worst-performing zones in terms of $LCOH^*$ (light-green and brown areas identified as H and G, respectively, in Fig. 8).

Table 5 presents the parameters' value ranges used to define each area, listing only the criteria relevant for area selection and omitting the value ranges of parameters not used as selection constraints for a specific area. For each area, a representative site was arbitrarily selected for showing the results of the sensitivity analysis. The specific parameters' values for these sites are provided in Table 6 while their locations are indicated in Fig. 8, marked by a star matching the area's color and labelled with the corresponding lowercase letter of the area identifier.

## 3. Results and discussion

This section presents the results of the method applied to the demonstrative case study of the northern Adriatic offshore area, covering both the eligibility assessment (*Subsection 3.1*) and the techno-economic spatially resolved assessment (*Subsections 3.2, 3.4,* and *3.5*), with particular attention to the influence of spatially dependent design variables (e.g., distance to ports and water depth). Specifically, *Subsection 3.2* examines the hydrogen producibility assessment, while Subsection 3.3 provides further insights into the effects of electrolyzer efficiency models on producibility. *Subsections 3.4* and *3.5* present the results concerning the spatial distribution of the system components' costs, the associated levelized costs of hydrogen (LCOH*), and the overall LCOH*. Finally, *Subsection 3.6* discusses the outcomes of the sensitivity analysis on the optimal electrolyzer size ratio.

**Table 5**
Parameters ranges for the selection of the scenarios area relevant to display the sensitivity $SR_{el}$ sensitivity analysis (empty positions for parameters not representing a selection criterion for that specific scenario).

| Scenario | d [m] | $D_p$ [km] | CF | LCOH [€/kg] |
|---|---|---|---|---|
| A Shallow water areas | 0–50 | 40.2–48.2 | 0.26–0.28 | – |
| B Deep water areas | 50–100 | 40.2–48.2 | 0.26–0.28 | – |
| C Near-ports areas | 0—100 | 8.0–16.0 | 0.26–0.28 | – |
| D Far-ports areas | 0—100 | 64.3–72.3 | 0.26–0.28 | – |
| E Low CF areas | 0—100 | 40.2–48.2 | 0.18–0.20 | – |
| F High CF areas | 0—100 | 40.2–48.2 | 0.34–0.36 | – |
| G High LCOH areas | – | – | – | 14–15 |
| H Low LCOH areas | – | – | – | 5–6 |

**Table 6**
Characteristics of the sites chosen for displaying the $SR_{el}$ sensitivity analysis. Coordinates are expressed in the EPSG:3035 LAEA Europe coordinate reference system.

| Sites | Scenario | North [m] | Est [m] | CF | $D_p$ [km] | d [m] |
|---|---|---|---|---|---|---|
| a | A | 2,513,837 | 4,601,968 | 0.27 | 43 | −46 |
| b | B | 2,345,837 | 4,670,968 | 0.27 | 44 | −65 |
| c | C | 2,417,837 | 4,611,968 | 0.28 | 14 | −43 |
| d | D | 2,374,837 | 4,578,968 | 0.26 | 66 | −49 |
| e | E | 2,442,837 | 4,562,968 | 0.20 | 45 | −33 |
| f | F | 2,292,837 | 4,738,968 | 0.35 | 42 | −100 |
| g | G | 2,267,837 | 4,673,968 | 0.23 | 72 | −91 |
| h | H | 2,402,837 | 4,623,968 | 0.33 | 19 | −48 |

### 3.1. Optimized domain

Based on the method and input data described in *Sections 2.3 and 2.8*, the exclusion areas identified from the processing of the layers listed in Table 2 were removed from the original domain to reduce the computational burden of the assessment (Fig. 9, left). As a result of this domain optimization, the number of analyzed cells was reduced by 44 %, with 24,632 cells processed out of 44,311 available in the sea domain, effectively saving nearly half of the computational effort. As illustrated in Fig. 9, the most significant exclusion constraints were distance from shore, heavily trafficked maritime areas, and environmentally protected zones.

### 3.2. Producibility maps

In Fig. 10 (top), the spatially resolved producibility map for $AHP^*$ is presented. Compared with Fig. 6, this map clearly illustrates the dependence on the $k^*$ and $A^*$ parameters of the Weibull probability density function (see Eq. (5)), which are the only intrinsically space-dependent physical factors influencing wind resource availability. The $AHP^*$ values range from 0.45 to 1.25 kt/y. In the same figure, three producibility hotspots were identified along the Croatian coast: one near the tip of the Istrian Peninsula, close to Pula harbor; another in the vicinity of the Kvarner and Dalmatian archipelagos; and a third in the southeastern portion of the spatial domain, likely extending beyond the boundaries of the computational area analyzed in this study. These locations represent a good spectrum of deployment conditions, spanning both shallow and deep waters and ranging extending from nearshore to far offshore. However, parts of these areas area excluded due to the imposed eligibility constraints (primarily distance to shore and ship traffic density), which substantially limit the potential of the identified hotspots.

### 3.3. Electrolyzer efficiency sensitivity analysis

The introduction of a real electrolyzer efficiency curve $\eta_{el}(v)$ into the producibility model increases $AHP^*$ estimates across the entire domain. This effect is shown in Fig. 10 (bottom left and right), which highlights how assuming a constant efficiency $\eta_{el}$ leads to an underestimation of producibility. Specific results for the representative scenarios and corresponding locations identified in Fig. 8 are provided in *Table S.6* of the *Supplementary Material*. The absolute producibility error, expressed as $\Delta AHP^*$ (i.e., the difference in $AHP^*$ between the constant $\eta_{el}$ and variable $\eta_{el}(v)$ cases), ranges between −6 and −30 t/year. The largest discrepancies occur when using the nominal efficiency $\eta_{el,nom}$ rather than the average efficiency $\eta_{el,ave}$.

This underestimation arises from the combined behavior of three elements: the Weibull distribution curve $f(v)^*$, the electrolyzer power curve $P_{el}(v)$, and $\eta_{el}(v)$ together with its constant approximations $\eta_{el,nom}$ and $\eta_{el,ave}$. Referring to Fig. 7 *(right)*, which displays $\eta_{el}(v)$ and its two constant approximation, three wind speed ranges can be identified where approximating $\eta_{el}(v)$ leads to overestimation or underestimation. Specifically:

- Low-v range (from $v_i$ to 4.5 m/s for $\eta_{el,nom}$, and to 4.75 m/s for $\eta_{el,ave}$) where both approximations overestimate $\eta_{el}(v)$;
- Middle-v range (from 4.5 to $v_{r,el}$ m/s for $\eta_{el,nom}$, and from 4.75 to $v_{r,el}$ m/s for $\eta_{el,ave}$) where both approximations underestimate $\eta_{el}(v)$;
- High-v range (from $v_{r,el}$ to $v_o$) where only $\eta_{el,ave}$ overestimates $\eta_{el}(v)$.

In the low-v range, the combined effect of high $f(v)^*$ (which typically peak in this range) and the strong overestimation of $\eta_{el}(v)$ is mitigated by the very low $P_{el}(v)$ which reduces the overall impact of $\eta_{el}(v)$ approximation. In the middle-v range, moderate-to-high $f(v)^*$ and $P_{el}(v)$ coincide with moderate underestimations of $\eta_{el}(v)$. Here, although the absolute approximation error is smaller than in the low-v range, its effect extends over a broader wind speed interval, producing a larger cumulative impact on total producibility. Lastly, in the high-v range, the overestimation introduced by $\eta_{el,ave}$ occurs at $P_{el,nom}$ (i.e., the maximum $P_{el}(v)$ value), but its influence is limited by the low probability values in the $f(v)^*$ tail. The combined effects of $f(v)^*$ and $P_{el}(v)$ emerge in the exemplifying annual energy consumption curves $AEC(v)^*$ of Fig. 5, which show that most of the $AEC^*$ (i.e., annual energy consumption corresponding to the area under the $AEC(v)^*$) is concentrated in the middle-v range where $\eta_{el}(v)$ is underestimated by the constant approximations. Consequently, the cumulative underestimation of producibility (see Eq. (14)) in this range outweighs the overestimation introduced by the use of $\eta_{el,nom}$ or $\eta_{el,ave}$ in the low-v ranges. Furthermore, when using $\eta_{el,ave}$, the additive overestimation at high v is still insufficient to offset the middle-v range underestimation. As a result, underestimation dominates in both approximation cases, with smaller $\Delta AHP^*$ values found for $\eta_{el,ave}$ (from –6 to –20 t/year) than for $\eta_{el,nom}$ (from –14 to –30 t/year).

Importantly, beyond the specifics of this case study, the impact of approximating $\eta_{el}(v)$ with constant values largely depends on the shape of the $f(v)^*$ curve. In particular, the more the Weibull peak shifts toward higher wind speeds, the stronger the influence of $\eta_{el}(v)$ underestimation in the middle-v range.

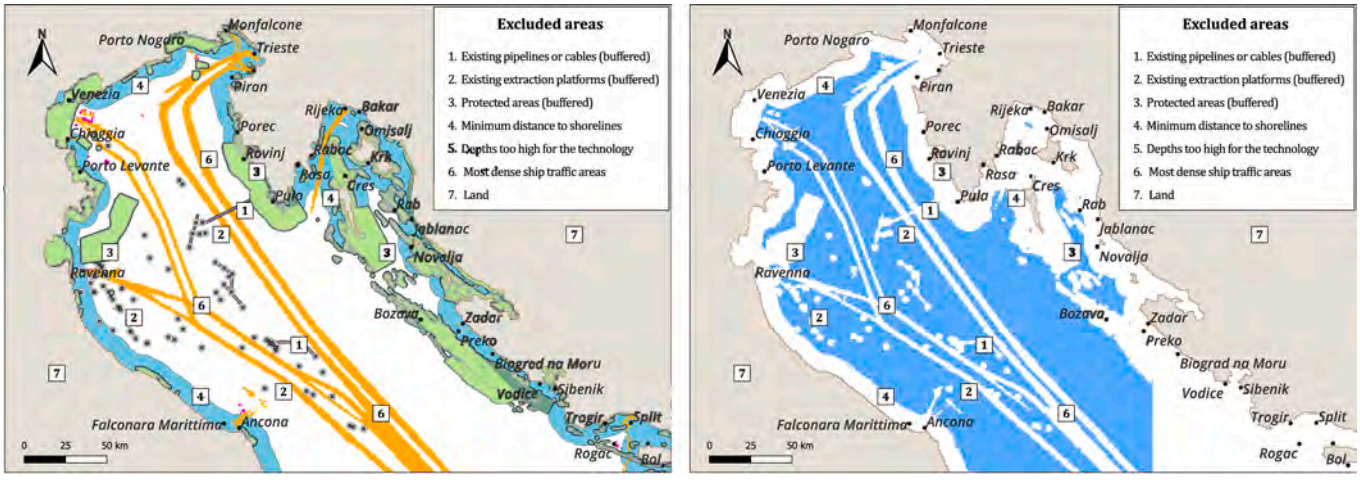


**Fig. 9.** Maps of the exclusion areas (left) and available areas (right) for the northernmost part of the Adriatic Sea.

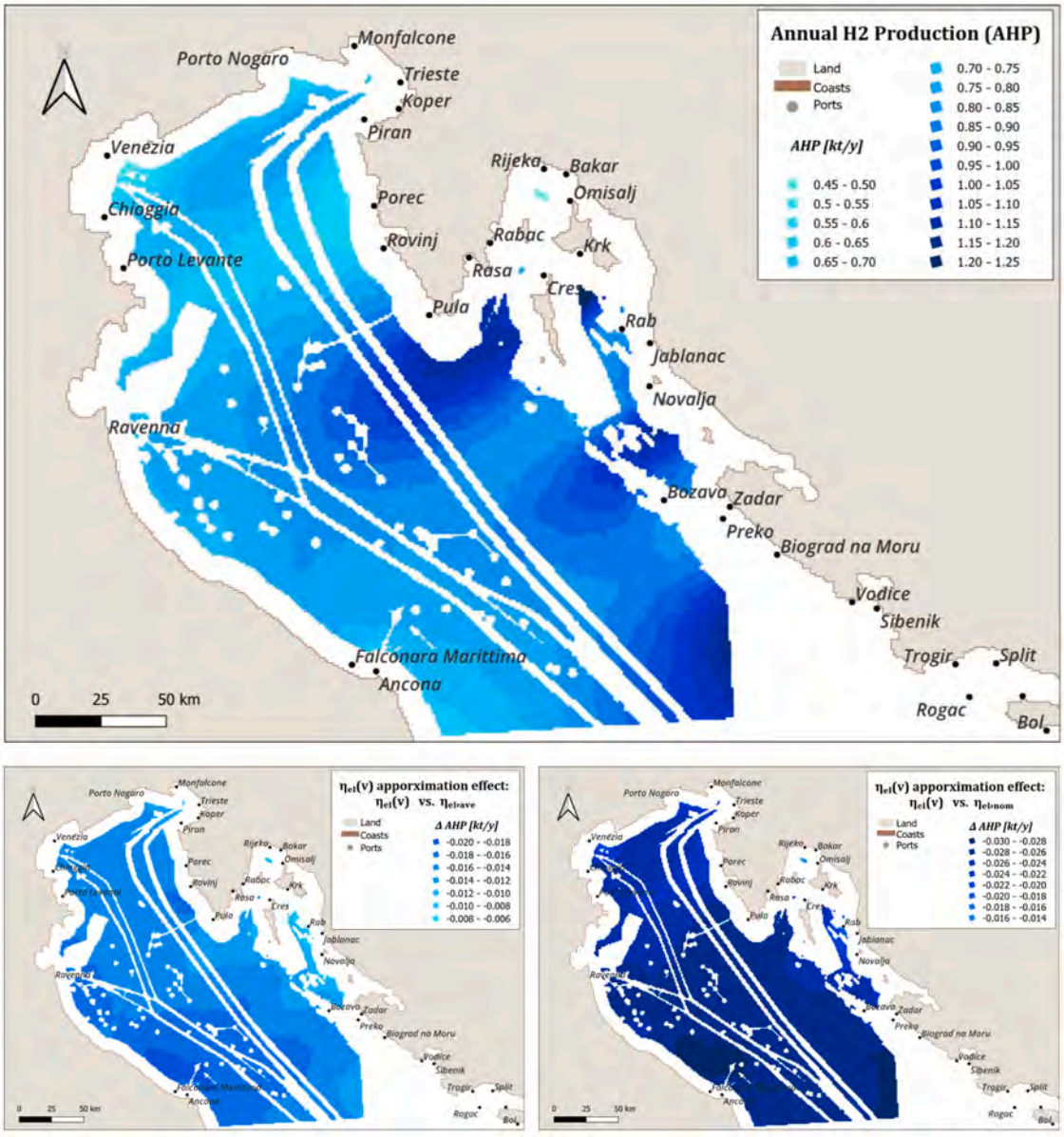


**Fig. 10.** Annual hydrogen production ($AHP^*$) map (top); Absolute error on the $AHP^*$ assessment when using $\eta_{el,ave}$ instead of $\eta_{el}(v)$ (bottom left); Absolute error on the $AHP^*$ assessment when using $\eta_{el,nom}$ instead of $\eta_{el}(v)$ (bottom right). All the results shown in the figure refer to wind farms with turbines spaced at minimum inter-turbine distances preventing interference effects between turbines.

This primarily dependence from $f(v)^*$ implies that the spatial distribution of $\Delta AHP^*$ is largely governed by the local values of the Weibull shape and scale parameters, $k^*$ and $A^*$. Indeed, the largest discrepancies occur where Weibull curves show low $A^*$ and high $k^*$ values, resulting in steeper peaks in the underestimation low-v range. Conversely, regions with high $A^*$ and medium $k^*$ values exhibit flatter curves, reducing underestimation effect on $AHP^*$. Therefore, the approximation impact is most pronounced in low-producibility areas, where steep Weibull curve peaks occur at low wind speeds (i.e., low $AEP^*$ zones).

This underestimation of $AHP^*$ also negatively affects $LCOH^*$, which, consistent with Eqs. (16) and (1), is overestimated yielding more pessimistic cost estimates. As further detailed in *Section 3.5*, this overestimation ranges from 0.05 to 0.55 €/kg, with the maximum error occurring when $\eta_{el,nom}$ is used.

### 3.4. Cost maps

The economic model is highly space dependent, with the most affected cost components being those related to the OWF and the gas pipeline. As shown in Fig. 11 (top right), the total pipeline cost $C^*_{pl}$ (including capital, operational and decommissioning expenditures, i.e., $CAPEX^*_{pl} + OPEX^*_{pl} + DECEX^*_{pl}$) primarily depends on $D^*_p$ (distance to port), exhibiting a linear relationship with a specific cost of 0.918 M€/km. Fig. 11 (top left) highlights the more heterogeneous behavior of $C^*_{WF}$ (total OWF cost including the wind farm capital, operational and decommissioning expenditures, i.e., $CAPEX^*_{WF} + OPEX^*_{WF} + DECEX^*_{WF}$). The spatial variability of $C^*_{WF}$ is driven by $D^*_p$ and $d^*$ (water depth), with $d^*$ having the dominant effect. Moving from shallow areas for bottom-fixed OWFs (about 57 M€ per system) to the deep with floating OWFs (about 81 M€ per system) results in an average cost increase of 24 M€. Moreover, $d^*$ seems to influence the dependence of $C^*_{WF}$ on $D^*_p$: in deeper

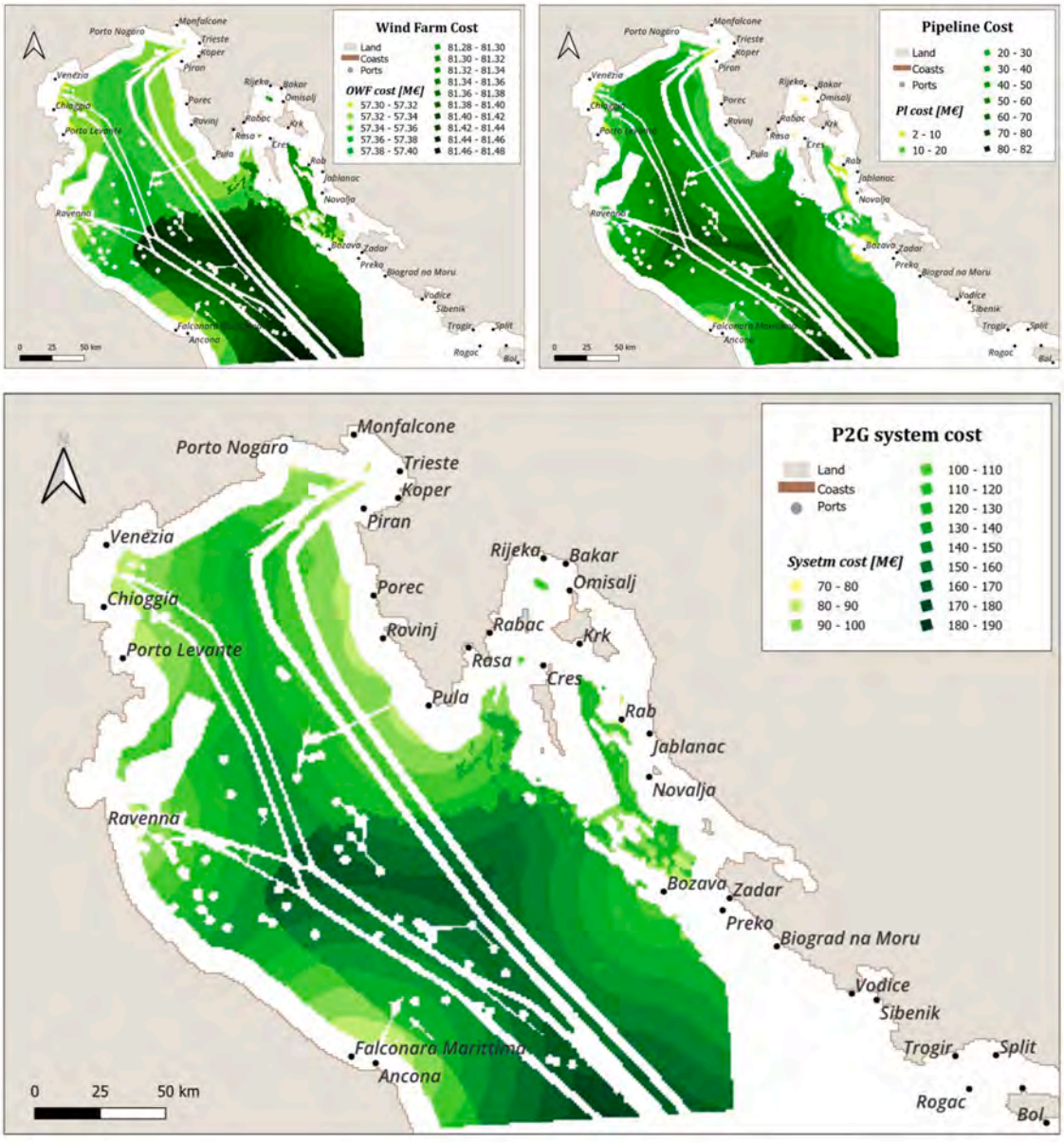


**Fig. 11.** Maps of spatially dependent costs: OWF-related costs (top-left); pipeline-related costs (top-right); and total P2G system costs (bottom).

waters, where substructures are more complex and their transportation costs are higher, the sensitivity to port distance becomes stronger, producing a steeper cost gradient as deeper sites move farther offshore.

The combined spatial effects of $C^*_{WF}$ and $C^*_{pl}$ are reported in Fig. 11 (bottom), where a pattern similar to that of $C^*_{WF}$ emerges, but with a stronger and more uniform influence of $D^*_p$. This is due to the dominant role of the $D^*_p$-related behavior of $C^*_{pl}$, whose absolute variation is generally almost two orders of magnitude larger than the $D^*_p$-related behavior of $C^*_{WF}$. Specifically, while the maximum difference in $C^*_{WF}$ between near-port and far-port sites (in both shallow and deep waters) is about 0.2 M€, the corresponding variation in $C^*_{pl}$ across the domain reaches roughly 80 M€.

The total system costs shares attributed to $C^*_{WF}$ and $C^*_{pl}$ range from 71 % and 3 % respectively in the best-case scenario, (shallow waters near ports) to 44 % for both in the worst-case scenario (far offshore and deep waters). This implies that the remaining share is covered by $C_{H2PP}$ (total $H_2$ production plant cost including the capital, operational and decommissioning expenditures, i.e., $CAPEX_{H2PP} + OPEX_{H2PP} + DECEX_{H2PP}$), which contributes up to 26 % in best-case locations (where electrolyzer related costs represent a larger fraction). The relatively small contribution of $C_{H2PP}$ partially explains the $SR_{el}$ sensitivity analysis results, presented in *Section 3.6*.

### 3.5. Levelized cost of hydrogen

The integration of the producibility and cost models enabled the evaluation of $LCOH^*$, whose spatial distribution is shown in Fig. 12 (top). The figure clearly highlights the strong influence of spatial dependencies on each $LCOH^*$ variable. Across the analyzed domain, $LCOH^*$ generally ranges between 5.0 and 15.0 €/kg, consistent with average values reported in the literature (2.0–16.0 €/kg [17,20,19,21]). In the best locations, offshore hydrogen production can even be competitive with onshore production (i.e., both PEMEL and wind farm sited onshore), which, according to [20], has average $LCOH^*$ value of 7€/kg for Portugal and Italy (ranging from 4 to 9 €/kg). As expected, the lowest values occur in areas with high energy potential, shallow waters

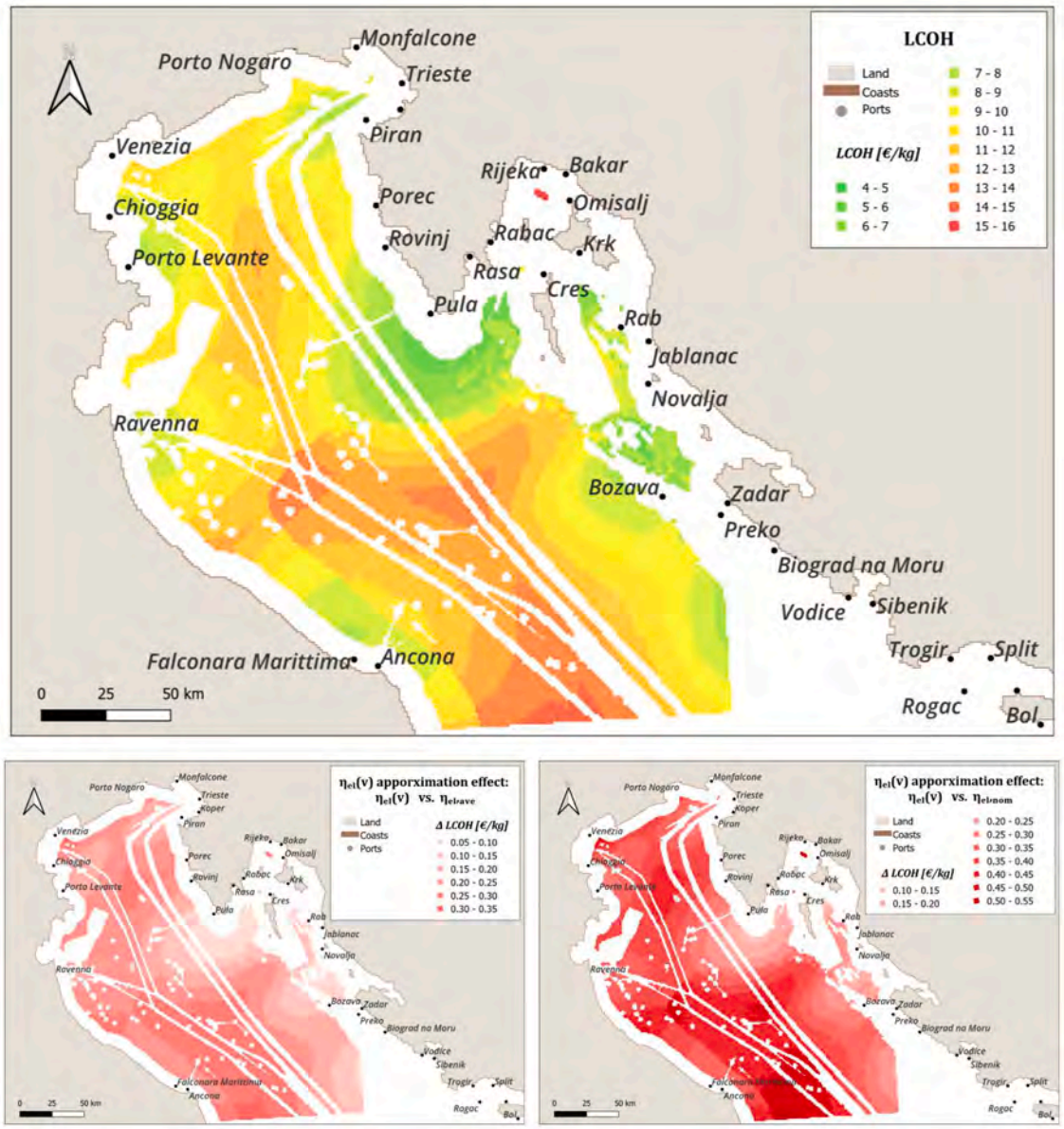


**Fig. 12.** Maps of the spatially dependent $LCOH^*$ delivered at the nearest suitable port, with the pipeline inside the system boundary (top); absolute error in $LCOH^*$ when using $\eta_{el,ave}$ instead of $\eta_{el}(v)$ (bottom-left); and absolute error in $LCOH^*$ when using $\eta_{el,nom}$ instead of $\eta_{el}(v)$ (bottom-right). Positive values of $\Delta LCOH$ describe overestimation.

and proximity to ports, which represent the optimal conditions for offshore electricity and hydrogen production. Specifically, the most promising areas lie off the Croatian coast near the ports of Pula, Bozava, Biograd na Moru and Vodice. The map also highlights that the most influential spatially-dependent parameters affecting $LCOH^*$ are the energy potential (i.e., $f(v)^*$ and $AHP^*$) and distance to port ($D_p^*$), whereas water depth ($d^*$) plays only a relatively secondary role. Indeed, the combination of high energy potential and short port distances can yield comparable best $LCOH^*$ values in both shallow and deep-water areas, making investments in deep sites with such characteristics competitive with those in shallower but less favorable regions.

This suggests that, under the techno-economic assumptions of this study, achieving substantial economic benefits from installing a P2G system in deep waters near a port suitable for manufacturing and O&M activities requires$AHP^* > 0.85$ kt/year. From this perspective, adapting the harbors of Pula, Bozava, Biograd na Moru, Ancona and Falconara Marittima for such purposes would represent the most strategic choice for offshore energy and P2G-oriented investments in the northern Adriatic Sea. For transparency, it is important to note that these results assume bottom based platforms for hosting offshore P2G facilities, regardless of $d^*$, due to the lack of literature data on the costs of offshore floating P2G hubs. Therefore, while the reliability of these findings is supported by the presence of existing bottom based extraction platforms in deep waters of the study area, further analysis including floating platform costs is recommended. However, within the total cost of the $H_2$ production plant ($C_{H2PP}$), the costs not associated with the electrolyzer (i.e., desalination, compressor and platform costs) account for only about 17 % of the total. Consequently, changing the platform assumption from bottom based to floating, is not expected to have a major impact on the results.

The strong dependence of $LCOH^*$ on $D_p^*$ makes the "distance to shore" exclusion parameter particularly relevant, as it removes economically favorable areas, especially near ports. However, in this specific domain, other exclusion constraints do not significantly reduce

the extent of favorable regions. Only the exclusion of major shipping lanes results in the loss of two offshore strips in the economically promising area near Pula harbor.

The impact of electrolyzer efficiency modeling assumptions on $LCOH^*$ is shown in Fig. 12 (bottom left and right) as the absolute deviations $\Delta LCOH^*$ obtained using constant efficiency approximations relative to the most realistic scenario (i.e., variable $\eta_{el}(v)$). Approximating $\eta_{el}(v)$ with a constant value leads to an overestimation of $LCOH^*$, resulting in less reliable estimates. Nevertheless, the absolute error remains moderate: it reaches a maximum of 0.55 €/kg in regions with the highest $LCOH^*$, while in the most economically favorable areas it does not exceed 0.1 and 0.25 €/kg when using $\eta_{el,ave}$ and $\eta_{el,nom}$, respectively.

Given the strong dependence of offshore $LCOH^*$ on $D_p^*$, the potential impact of retrofitting an existing gas pipeline for hydrogen transport was assessed. As noted in *Section 2.8*, in this analysis, the existing pipeline was treated as a potential landing point for newly constructed $H_2$ pipelines, and three different retrofitting costs scenarios were considered: no retrofitting cost, medium-cost retrofitting, and high-cost retrofitting. As shown in Fig. 13, the most favorable scenario is the one assuming zero retrofitting cost (i.e., 0 M€/km). This assumption yields substantial benefits across an area of approximately 6,000 $km^2$ (24 % of the optimized domain) and leads to a maximum average $LCOH^*$ reduction of 2 €/kg. Notably, in areas closest to the retrofitted pipeline, the reduction can reach up to 4 €/kg. Since retrofitting costs are excluded in this scenario, these results should be considered as the lower bound of potential $LCOH^*$ benefits in retrofitting scenarios. Indeed, given the limitation that existing pipelines can only be used as-is to transport natural gas–hydrogen mixtures with a volumetric hydrogen share below 10 %, the results change when blends with hydrogen shares above 10 % or pure hydrogen are considered. Specifically, in the medium-cost scenario (middle panel of Fig. 13), the assumed retrofitting specific cost narrows the affected area and reduces the average $LCOH^*$ improvement by nearly 50 % (from 6,000 $km^2$ to 3,250 $km^2$ and from 2 €/kg to 1 €/kg), with maximum $LCOH^*$ reductions of 3 €/kg near the existing pipeline. When the retrofitting specific cost is further increased (high-cost scenario, bottom panel of Fig. 13), the extent of the benefited area shrinks drastically to a narrow band of sites farther from the nearby ports (255 $km^2$), and the $LCOH^*$ reduction becomes almost negligible (0.17 €/kg on average, with only a few peaks between 0.25–0.5 €/kg). These results clearly indicate that retrofitting existing pipelines is generally not advantageous when costs approach those of the high-cost scenario (0.546 M€/km) unless the risks of retrofitting and operating an existing pipeline are deemed lower than those associated with constructing and operating a new, more versatile pipeline. It should also be noted that for both the medium- and high-cost scenarios, the impact of retrofitting on $LCOH^*$ is conservative, as in the present analysis the entire retrofitting investment for the pipeline section between the injection point and landing point is allocated to the single 20 MW P2G plant associated with each evaluated cell. In practice, if multiple P2G systems were installed simultaneously in locations favorable for connection to the existing pipeline, or if larger P2G systems were considered, the retrofit investment (for the shared section or entire relevant segment) would be distributed among several plants. This cost-sharing effect would further mitigate the impact of retrofitting on $LCOH^*$, potentially making the connection economically viable even in areas that appear unfavorable under the present scenarios. However, the extent of the impacted area would never exceed that observed under the most favorable zero-cost scenario (see top panel of Fig. 13).

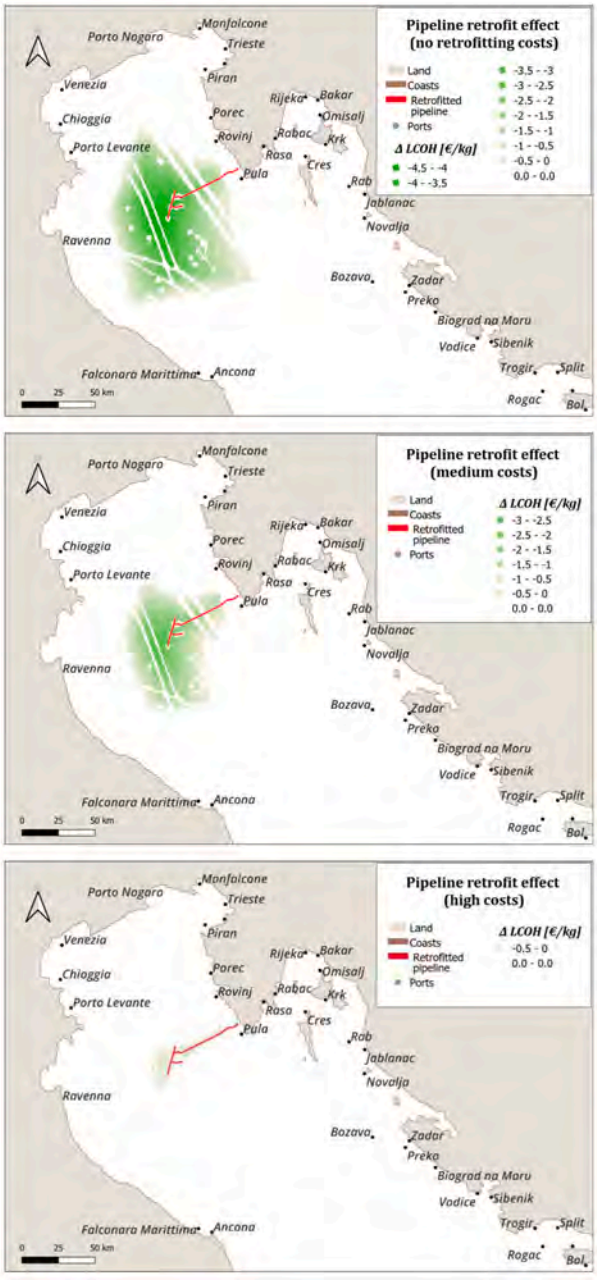


**Fig. 13.** Improvement in $LCOH^*$ values when considering the availability of a retrofitted pipeline. From top to bottom: improvement when retrofitting costs are assumed to be 0 (this case represents the lowest bound for the potential decrease of $LCOH^*$ in retrofitting scenarios); improvement when assuming medium retrofitting specific costs (equal to 10 % of the cost of an equivalent new hydrogen pipeline [46]); improvement when assuming high retrofitting specific costs (0.546 M€/km [15]).

### 3.6. Size ratio sensitivity analysis

As discussed in Section 2.7, a sensitivity analysis was performed to evaluate the optimal ratio between PEMEL size and OWF size (i.e., $SR_{el,opt}$). To verify the consistency of the results across the optimized spatial domain, a detailed assessment of the sensitivity analysis outcomes was conducted for a selection of representative sites located within the areas identified using the method described in *Section 2.8*. These areas, selected by imposing ranges on four spatially dependent parameters ($d^*$, $D_p^*$, $CF^*$ and $LCOH^*$), are shown in Fig. 8 together with their representative sites. It should be noted that not all theoretical combinations of $d^*$, $D_p^*$, and $CF^*$ occur within the studied domain, in either shallow or deep waters. However, this limitation does not compromise the completeness of the study, as representative areas for all combinations of $D_p^*$ and $CF^*$ were found at least once in either shallow or

deep water. Since the impact of $d^*$ on costs (and thus on $LCOH^*$) is constant between shallow and deep sites (with a difference of about 24 M€, see Fig. 11 top-left), results for the missing theoretical combinations can be reliably extrapolated. Accordingly, the costs of missing deep-water scenarios can be obtained by adding 24 M€ to the P2G system costs estimated for shallow-water scenarios, whereas those of missing shallow-water scenarios can be derived by subtracting the same amount from the corresponding deep-water scenario costs. The sensitivity analysis results are presented in Figs. 14–16.

Fig. 14 shows the influence of varying the size ratio ($SR_{el}$) on $LCOH^*_{H2PP}$ (i.e., the component of $LCOH^*$ associated solely with H2PP costs, left) and on total $LCOH^*$ (right). A comparison of $LCOH^*_{H2PP}$ across the analyzed sites reveals its independence from $d^*$ and $D^*_p$, as these parameters are not involved in the definition of $C_{H2PP}$ ($H_2$ production plant costs). Consequently, the curves for sites a, b, c, and d show no significant differences. In contrast, $CF^*$ affects $LCOH^*_{H2PP}$ through its influence on $THP^*$, leading to lower costs in the most productive sites (i.e., sites f and h). When analyzing total $LCOH^*$ (Fig. 14 right), the relative influence of $d^*$, $D^*_p$, and $CF^*$ aligns with the findings discussed in *Section 3.5* (Fig. 12, top). The strongest spatial dependency is associated with variations in $D^*_p$, with a difference for optimal $LCOH^*$ of about 4 €/kg between sites c (closer to port and more favorable) and d. Conversely, the effects of $CF^*$ and $d^*$ are less pronounced, with $d^*$ having a slightly greater impact than $CF^*$. Specifically, the 2 €/kg difference between site b and the shallower, more favorable site a is slightly larger than the 1.7 €/kg difference between site e, characterized by lower $CF^*$, and site f (excluding the depth effect in the latter pair). All these differences in *LCOH* values among the contrasting sites are clearly visible in Fig. 14 right panel (especially in the zoomed view).

The behavior of $LCOH^*_{H2PP}$ confirms, in all cases, the existence of an optimal $SR_{el}$ lower than 1, and thus an optimal PEMEL size. This optimal $SR_{el}$ appears to increase with $CF^*$, as shown by the progressive flattening of the $LCOH^*_{H2PP}$ curve for sites f and h, resulting in a higher optimal $SR_{el}$ at site h than at the other sites (0.15 versus 0.05).

However, Fig. 14 right shows that this optimum for $LCOH^*_{H2PP}$ does not affect the behavior of total $LCOH^*$, which decreases monotonically from smaller PEMEL sizes to the size corresponding to the wind farm nominal capacity (i.e., $SR_{el} = 1$). This means that, across all analyzed sites (i.e., all combinations of the considered parameters), the optimal $SR_{el}$ for minimizing $LCOH^*$ is 1 (i.e., $P_{el,nom} = WF_c$). This finding is significant, as it diverges from onshore results reported in [41] and shows a slight deviation from what found in [20] and [21], despite confirming that for offshore applications the optimal $SR_{el}$ remains close to 1 due to the higher costs of OWFs. The underlying reason lies in the relative magnitude of system cost components, as shown in Fig. 15 and Fig. 16, which focus on the locations with the best and worst of $LCOH_{H2PP}$ and LCOH values in Fig. 14. In all cases, even when excluding gas transport costs (which strongly affect total costs, as shown in Fig. 11), the dominant total cost driver throughout the sensitivity analysis remains $C_{WF}$. This holds regardless of $d^*$, making the contribution of $C_{H2PP}$ marginal in determining total LCOH. The limited role of $LCOH_{H2PP}$ is further emphasized in Fig. 15, which breaks down LCOH for the same sites analyzed in Fig. 16. The relatively low PEMEL cost contribution also reflects the specific cost function used for PEMEL CAPEX estimation (see Eq. (34)[47]), which yields lower specific costs than those assumed in [20] and [21], while remaining realistic and consistent with current market data.

To identify the $SR_{el}$ values that keep $LCOH^*$ within 5 % of its optimum, the zoomed view in Fig. 14 right panel highlights the near-optimum bands. These define, for each scenario, the $SR_{el}$ intervals in which $LCOH^*$ remains within 5 % above its minimum. Owing to the flattening of $LCOH^*(SR_{el})$ curves between$SR_{el} = 0.70$–1 across all scenarios, the $SR_{el}$ values ensuring a +5 % near-optimum consistently fall within 0.82–0.89. This indicates that, within the $SR_{el}$ range 0.82–1, downsizing the electrolyzer has only a marginal influence on $LCOH^*$. Nonetheless, although selecting a $SR_{el}$ that keeps $LCOH^*$ within +5 % may represent a reasonable compromise to reduce electrolyzer investment costs, the resulting economic gain may be insufficient to compensate for the reduced hydrogen producibility for$SR_{el} < 1$. These considerations suggest avenues for future, more targeted analyses.

## 4. Conclusions

This study developed and tested a GIS-based method to evaluate the spatially resolved levelized cost of hydrogen (LCOH) delivered onshore from offshore centralized power to gas systems, with the northern Adriatic Sea serving as a case study.

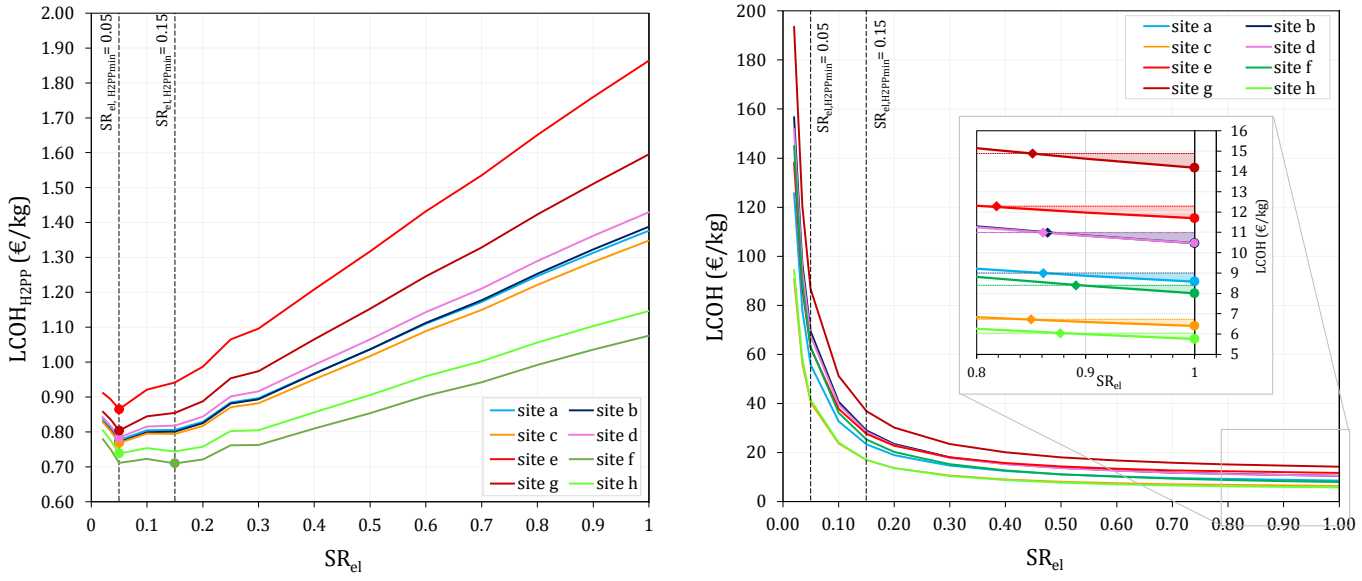


**Fig. 14.** $SR_{el}$ sensitivity analysis results: behaviors of $LCOH_{H2PP}$ (left) and total LCOH at port (right) for the selected sites. On the right, a zoom on the optimal LCOH values highlights the colored near-optimum bands, which show the LCOH values within + 5 % of the optimum and the corresponding $SR_{el}$ values for each site. The sites are graphically represented in Fig. 8 and described in Table 6.

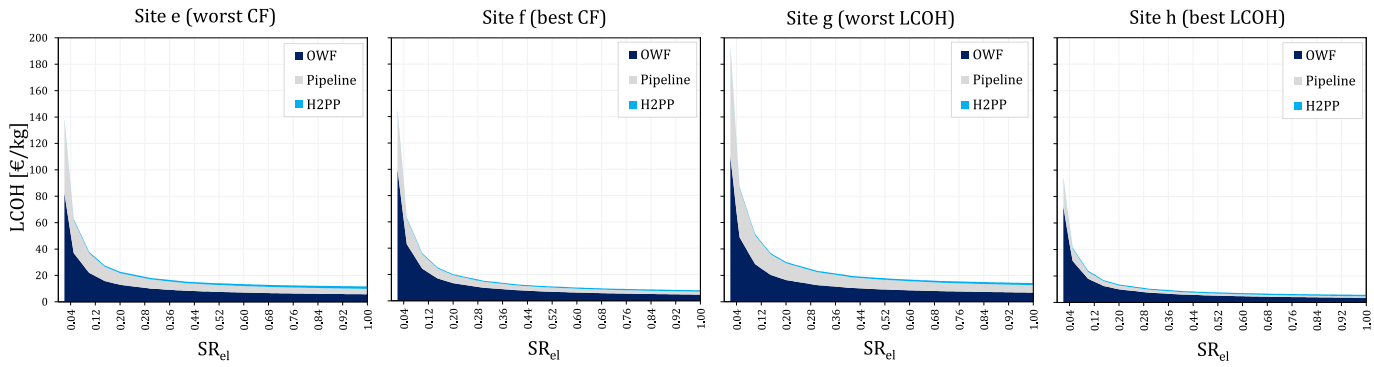


**Fig. 15.** Composition of the total LCOH at port as a function of $SR_{el}$ for the four sites representing the best and worst values of $LCOH_{H2PP}$ and LCOH. Blue, grey and azure areas indicate the respective contribution of OWF, pipeline and H2PP costs to the total LCOH across the sensitivity analysis.

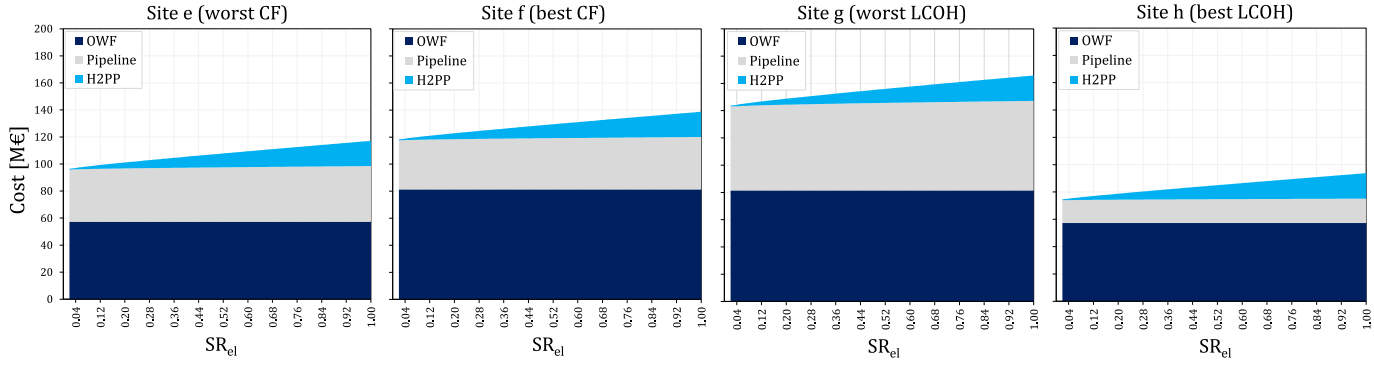


**Fig. 16.** Composition of the total cost per system as a function of $SR_{el}$ for the four sites representing the best and worst values of $LCOH_{H2PP}$ and LCOH. Blue, grey and azure areas indicate the respective contribution of OWF ($C^*_{WF}$), pipeline ($C^*_{pl}$), and H2PP ($C_{H2PP}$) costs to the total cost across the sensitivity analysis.

Integrating an analytical producibility assessment with a preliminary GIS-based eligibility analysis ensured accurate calculations and results interpretations, while also improving computational efficiency. By focusing the analysis on an optimized domain, overall computational effort was reduced by over 40 %. Well-grounded and deliberate application of exclusion constraints permitted the removal of areas that, while favorable in terms of LCOH, were not realistically exploitable due to environmental, legal, or public-acceptance rules, thereby ensuring results that better reflect real-world feasibility.

Alongside the development of the method, key insights on modeling assumptions were obtained through two sensitivity analyses:

- The first addressing the modeling of the electrolyzer efficiency $\eta_{el}(v)$, comparing results obtained using a variable (non-constant) efficiency curve against those based on two constant representative values: the nominal efficiency ($\eta_{el,nom}$) and the average efficiency ($\eta_{el,ave}$). The findings clearly indicate that, generally, by using a constant value for approximating $\eta_{el}(v)$, the producibility of hydrogen is underestimated leading to a consequent overestimation of the LCOH$^*$. However, although a variable $\eta_{el}(v)$ should ideally be used for accuracy, the use of $\eta_{el,ave}$ offers a reasonable and more reliable approximation than $\eta_{el,nom}$ when computational simplicity is required.
- The second examining the optimal electrolyzer sizing ratio $SR_{el}$, which represents the cost-optimal electrolyzer size relative to the fixed offshore wind farm (OWF) capacity. The results showed that, unlike onshore applications and contrary to some prior studies, the optimal $SR_{el}$ for offshore settings consistently equals 1 (i.e., the economically optimal electrolyzer capacity always matches the nominal capacity of the OWF). This outcome is primarily attributed to the significantly higher cost of offshore wind infrastructure compared to that of the electrolyzer. However, $SR_{el}$ values ensuring near-optimal LCOH within + 5 % of its minimum fall consistently in the range 0.89–1 allowing a saving in terms of electrolyzer CAPEX of the order of magnitude of 1 M€. The study of the convenience of such economic savings in comparison to the effects of loss of hydrogen production could stimulate future, more targeted research.

Applying the method to the northern Adriatic Sea revealed that the distance to port $D_p^*$ and energy availability (represented by the Weibull distribution $f(v)^*$ and corresponding capacity factor CF$^*$) are the most influential spatial parameters affecting LCOH$^*$. In fact, although water depth remains a significant parameter influencing the LCOH, its impact can be mitigated in areas characterized by favorable combinations of high resource availability (high CF$^*$) and proximity to ports. The lowest LCOH$^*$ values (around 5 €/kg) were found in limited zones characterized by these conditions, demonstrating to be competitive in some cases with levelized cost of completely on-land produced hydrogen.

Finally, an initial assessment of the potential impact and prospective interest in reusing natural gas pipelines for hydrogen transport was conducted, proving such a strategy to be effective in reducing transportation costs particularly under zero-cost or medium-cost retrofitting cost assumptions. In the most favorable areas (i.e., those close to existing pipeline infrastructure), the LCOH was reduced by up to 4 €/kg in the zero-cost scenario and 3 €/kg in the medium-cost scenario. Although preliminary, these results indicate promising benefits. Nevertheless, more detailed and comprehensive analyses are required to validate these findings. Future work should therefore focus on developing more accurate retrofitting cost models and, especially under high specific retrofitting costs, on assessing both the risks and the advantages of pipeline retrofitting in comparison with the construction and operation of new submarine gas pipelines.

Given the intended scope of this kind of high-level assessment, future research could focus on coupling the proposed framework with energy system optimization models by incorporating the georeferenced characterization of offshore energy and hydrogen maximum production potentials as boundary conditions. This approach would enhance the accuracy of the optimized models by taking advantage of the spatial resolution of the input data.

## CRediT authorship contribution statement

**Alberto Ferrarese:** Writing – review & editing, Writing – original draft, Visualization, Validation, Software, Resources, Methodology, Investigation, Formal analysis, Data curation, Conceptualization. **Paolo Marocco:** Writing – review & editing, Supervision, Project administration, Methodology, Investigation, Conceptualization. **Giuliana Mattiazzo:** Supervision, Funding acquisition. **Massimo Santarelli:** Writing – review & editing, Supervision, Project administration, Funding acquisition.

## Declaration of competing interest

The authors declare that they have no known competing financial interests or personal relationships that could have appeared to influence the work reported in this paper.

## Acknowledgments

“This publication is part of the project PNRR-NGEU which has received funding from the MUR – DM 351/2022”.

## Appendix A. Supplementary data

Supplementary data to this article can be found online at https://doi.org/10.1016/j.enconman.2025.120948.

## Data availability

Data will be made available on request.

## References

[1] IEA (International Energy Agency), “Wind power capacity in the net zero scenario 2015-2030,” IEA (2023), Wind power capacity in the Net Zero Scenario, 2015-2030, IEA, Paris. Accessed: Nov. 12, 2024. [Online]. Available: https://www.iea.org/data-and-statistics/charts/wind-power-capacity-in-the-net-zero-scenario-2015-2030.
[2] IEA (International Energy Agency), “Renewables 2024,” 2024. [Online]. Available: www.iea.org.
[3] European Commission, “COMMUNICATION FROM THE COMMISSION TO THE EUROPEAN PARLIAMENT, THE COUNCIL, THE EUROPEAN ECONOMIC AND SOCIAL COMMITTEE AND THE COMMITTEE OF THE REGIONS A hydrogen strategy for a climate-neutral Europe,” 2020. [Online]. Available: https://www.eu2018.at/calendar-events/political-events/BMNT-.
[4] IEA (International Energy Agency), “Global Hydrogen Review 2024,” 2024. [Online]. Available: www.iea.org.
[5] IRENA (International Renewable Energy Agency), *Green hydrogen cost reduction : scaling up electrolysers to meet the 1.5°C climate goal*. 2020. Accessed: Dec. 08, 2025. [Online]. Available: www.irena.org/publications.
[6] Hydrogen Council, “Path to hydrogen competitiveness A cost perspective,” 2020. [Online]. Available: www.hydrogencouncil.com.
[7] J. Incer-Valverde, A. Korayem, G. Tsatsaronis, and T. Morosuk, “‘Colors’ of hydrogen: Definitions and carbon intensity,” Sep. 01, 2023, *Elsevier Ltd*. https://doi.org/10.1016/j.enconman.2023.117294.
[8] Marocco P, et al. A study of the techno-economic feasibility of H2-based energy storage systems in remote areas. Energy Convers Manag May 2020;211. https://doi.org/10.1016/j.enconman.2020.112768.
[9] Douadi O, Ravi R, Faqir M, Balasubramanian D, Kale U, Kilikevičius A. A study on zero-emission vehicle technologies: comparing hydrogen fuel cell and battery electric solutions for decarbonization of transportation. Thermal Sci Eng Prog Oct. 2025;66:103990. https://doi.org/10.1016/J.TSEP.2025.103990.
[10] R. Lago Sari, A. Fogue Robles, J. Monsalve Serrano, D. Cleary, Techno-economic assessment of hydrogen as a fuel for internal combustion engines and proton exchange membrane fuel cells on long haul applications, Energy Convers Manag, 311, 118522, Jul. 2024, https://doi.org/10.1016/J.ENCONMAN.2024.118522.
[11] IEA (International Energy Agency), Global Hydrogen Review 2021, 2021. [Online]. Available: www.iea.org/t&c/.
[12] Hydrogen Council and McKinsey & Company, Hydrogen for Net-Zero, 2021. [Online]. Available: www.hydrogencouncil.com.
[13] IEA (International Energy Agency), Offshore Wind Outlook 2019: World Energy Outlook Special Report. [Online]. Available: www.iea.org/t&c/.
[14] Song S, et al. Production of hydrogen from offshore wind in China and cost-competitive supply to Japan. Nat Commun 2021;12(1):Dec. https://doi.org/10.1038/s41467-021-27214-7.
[15] V. Juárez-Casildo, I. Cervantes, R. de G. González-Huerta, Harnessing offshore wind for decarbonization: A geospatial study of hydrogen production and heavy industry utilization in Mexico, Int J Hydrogen Energy, 83, 701–716, Sep. 2024, https://doi.org/10.1016/j.ijhydene.2024.08.142.
[16] Lucas TR, Ferreira AF, Santos Pereira RB, Alves M. Hydrogen production from the WindFloat Atlantic offshore wind farm: a techno-economic analysis. Appl Energy 2022;310:Mar. https://doi.org/10.1016/j.apenergy.2021.118481.
[17] QV Dinh, VN Dinh, H Mosadeghi, PH Todesco Pereira, PG Leahy, A geospatial method for estimating the levelised cost of hydrogen production from offshore wind, Int J Hydrogen Energy, 48, 40, 15000–15013, May 2023, https://doi.org/10.1016/j.ijhydene.2023.01.016.
[18] Giampieri A, Ling-Chin J, Roskilly AP. Techno-economic assessment of offshore wind-to-hydrogen scenarios: a UK case study. Int J Hydrogen Energy Jan. 2024;52:589–617. https://doi.org/10.1016/j.ijhydene.2023.01.346.
[19] Rogeau A, Vieubled J, de Coatpont M, Affonso Nobrega P, Erbs G, Girard R. Techno-economic evaluation and resource assessment of hydrogen production through offshore wind farms: a European perspective. Renew Sustain Energy Rev 2023;187:Nov. https://doi.org/10.1016/j.rser.2023.113699.
[20] Vidas L, Castro R, Bosisio A, Pires A. Optimal sizing of renewables-to-hydrogen systems in a suitable-site-selection geospatial framework: the case study of Italy and Portugal. Renew Sustain Energy Rev Sep. 2024;202. https://doi.org/10.1016/j.rser.2024.114620.
[21] Zhou Z, Cai G, Huang Y, Bai R, Nie S, Chen X. Spatial and temporal evolution of cost-competitive offshore hydrogen in China: a techno-economic analysis. Renew Sustain Energy Rev Oct. 2024;203. https://doi.org/10.1016/j.rser.2024.114780.
[22] Komorowska A, Benalcazar P, Kamiński J. Evaluating the competitiveness and uncertainty of offshore wind-to-hydrogen production: a case study of Poland. Int J Hydrogen Energy May 2023;48(39):14577–90. https://doi.org/10.1016/j.ijhydene.2023.01.015.
[23] JW Ding, YS Fu, IY Lisa Hsieh, The cost of green: analyzing the economic feasibility of hydrogen production from offshore wind power, Energy Conver Manage: X, vol. 24, Oct. 2024, https://doi.org/10.1016/j.ecmx.2024.100770.
[24] Singlitico A, Østergaard J, Chatzivasileiadis S. Onshore, offshore or in-turbine electrolysis? Techno-economic overview of alternative integration designs for green hydrogen production into Offshore Wind Power Hubs. Renew Sustain Energy Transit Aug. 2021;1. https://doi.org/10.1016/j.rset.2021.100005.
[25] Wulf C, Linssen J, Zapp P. Power-to-gas-concepts, demonstration, and prospects, in Hydrogen Supply Chain: Design. Deployment and Operation, Elsevier 2018:309–45. https://doi.org/10.1016/B978-0-12-811197-0.00009-9.
[26] Meier K. Hydrogen production with sea water electrolysis using norwegian offshore wind energy potentials: techno-economic assessment for an offshore-based hydrogen production approach with state-of-the-art technology. Int J Energy Environ Eng Jul. 2014;5(2–3):1–12. https://doi.org/10.1007/s40095-014-0104-6.
[27] Scolaro M, Kittner N. Optimizing hybrid offshore wind farms for cost-competitive hydrogen production in Germany. Int J Hydrogen Energy Feb. 2022;47(10):6478–93. https://doi.org/10.1016/j.ijhydene.2021.12.062.
[28] Franco BA, Baptista P, Neto RC, Ganilha S. Assessment of offloading pathways for wind-powered offshore hydrogen production: energy and economic analysis. Appl Energy Mar. 2021;286. https://doi.org/10.1016/j.apenergy.2021.116553.
[29] Jang D, Kim K, Kim KH, Kang S. Techno-economic analysis and Monte Carlo simulation for green hydrogen production using offshore wind power plant. Energy Convers Manag Jul. 2022;263. https://doi.org/10.1016/j.enconman.2022.115695.
[30] Dinh QV, Dinh VN, Leahy P. A method to map the levelised cost of hydrogen from offshore wind farms coupled to onshore electrolysers via HVDC. IOP Conf Ser: Earth Environ Sci Inst Phys 2023. https://doi.org/10.1088/1755-1315/1281/1/012005.
[31] Hill SJP, Bamisile O, Hatton L, Staffell I, Jansen M. The cost of clean hydrogen from offshore wind and electrolysis. J Clean Prod Mar. 2024;445. https://doi.org/10.1016/j.jclepro.2024.141162.
[32] QGIS Development Team, “QGIS Geographic Information System. Open Source Geospatial Foundation Project.,” 2023, 3.28.3. Accessed: Jun. 01, 2024. [Online]. Available: http://qgis.osgeo.org.
[33] RSE- Ricerca Sistema Energetico, “AEOLIAN- Atlante EOlico ItaliANo.” Accessed: Oct. 01, 2024. [Online]. Available: https://atlanteeolico.rse-web.it/html/download_terria_griglia-IT.html.
[34] European Commission, “EMODnet (European Marine Observation and Data network) map viewer.” Accessed: Oct. 01, 2024. [Online]. Available: https://emodnet.ec.europa.eu/geoviewer/#!/.
[35] UNESCO - IHO (International Hydrographic Organization), “GEBCO (GEneral Bathymetric Chart of the Ocean) - Gridded Bathymetry Data.” Accessed: Oct. 01, 2024. [Online]. Available: https://www.gebco.net/data_and_products/gridded_bathymetry_data/.
[36] Moore A, Price J, Zeyringer M. The role of floating offshore wind in a renewable focused electricity system for Great Britain in 2050. Energy Strategy Rev Nov. 2018;22:270–8. https://doi.org/10.1016/j.esr.2018.10.002.

[37] Ç. Karar Verme Metodu Kullanarak Bandırma Körfezinde Uygun Deniz Üstü Rüzgar Enerji Santral Alanlarının Tespiti *et al.*, "Sorumlu Yazar/Corresponding Author Determining Suitable Regions for Potential Offshore Wind Farms in Bandırma Bay using Multi-criteria-Decision-Making Method," 2020.
[38] Tlili O, et al. Downscaling of future national capacity scenarios of the French electricity system to the regional level. Energy Syst Feb. 2022;13(1):137–65. https://doi.org/10.1007/s12667-020-00406-8.
[39] B. Möller Bernd, Continuous spatial modelling to analyse planning and economic consequences of offshore wind energy, Energy Policy, 39, 2, 511–517, Feb. 2011, https://doi.org/10.1016/j.enpol.2010.10.031.
[40] C. E. magazine Vatavuk W. M., "Chemical Engineering Plant Cost Index," Updating the CE Plant Cost Index, Chemical Engineering.
[41] Marocco P, Gandiglio M, Cianella R, Capra M, Santarelli M. Design of hydrogen production systems powered by solar and wind energy: an insight into the optimal size ratios. Energy Convers Manag Aug. 2024;314. https://doi.org/10.1016/j.enconman.2024.118646.
[42] J Jonkman, S Butterfield, W Musial, G Scott, "Definition of a 5-MW Reference Wind Turbine for Offshore System Development," 2009. [Online]. Available: http://www.osti.gov/bridge.
[43] Marcogaz AISBL, "Overview of available test results* and regulatory limits for hydrogen admission into existing natural gas infrastructure and end use Infographic Version 2023." [Online]. Available: www.marcogaz.org.
[44] Hydrogen Europe, "| Hydrogen Infrastructure Report 2 Contents.".
[45] ACER (European Union Agency for the Cooperation of Energy Regulators), "Transporting Pure Hydrogen by Repurposing Existing Gas Infrastructure: Overview of existing studies and reflections on the conditions for repurposing," Ljubljana, Slovenia, 2021.
[46] Martínez-Gordón R, Gusatu L, Morales-España G, Sijm J, Faaij A. Benefits of an integrated power and hydrogen offshore grid in a net-zero North Sea energy system. Adv Appl Energy Sep. 2022;7. https://doi.org/10.1016/j.adapen.2022.100097.
[47] Reksten AH, Thomassen MS, Møller-Holst S, Sundseth K. Projecting the future cost of PEM and alkaline water electrolysers; a CAPEX model including electrolyser plant size and technology development. Int J Hydrogen Energy Nov. 2022;47(90):38106–13. https://doi.org/10.1016/j.ijhydene.2022.08.306.
[48] D. Miriello, M. Walker, A. Smith, and D. Roddier, "Design and inclusion of a desalination system in a floating offshore wind farm OMAE2019-95024," 2019. [Online]. Available: http://asmedigitalcollection.asme.org/OMAE/proceedings-pdf/OMAE2019/58837/V006T05A034/6443613/v006t05a034-omae2019-95024.pdf.
[49] "European Hydrogen Backbone HOW A DEDICATED HYDROGEN INFRASTRUCTURE CAN BE CREATED," 2020. [Online]. Available: https://transparency.entsog.eu/.